PMAS: The Potsdam Multi-Aperture Spectrophotometer. I. Design, Manufacture, and Performance

MARTIN M. ROTH,[1,2] ANDREAS KELZ,[1] THOMAS FECHNER, THOMAS HAHN, SVEND-MARIAN BAUER, THOMAS BECKER,[1,2]
PETRA BÖHM,[1] LISE CHRISTENSEN,[1] FRANK DIONIES, JENS PASCHKE, EMIL POPOW, AND DIETER WOLTER

Astrophysikalisches Institut Potsdam, An der Sternwarte 16, D-14482 Potsdam, Germany; mmroth@aip.de

JÜRGEN SCHMOLL[1,2]

Astronomical Instrument Group, Department of Physics, University of Durham, Rochester Building, South Road, Durham DH1 3LE, UK

UWE LAUX[3]

Thüringer Landessternwarte Tautenburg, Sternwarte 5, Tautenburg D-07778, Germany

AND

WERNER ALTMANN[3]

Konstruktionsbüro Altmann, Passau, Germany

ABSTRACT. We describe the design, manufacture, commissioning, and performance of PMAS, the Potsdam Multi-Aperture Spectrophotometer. PMAS is a dedicated integral field spectrophotometer optimized to cover the optical wavelength regime of 0.35–1 μm. It is based on the lens array–fiber bundle principle of operation. The instrument employs an all-refractive fiber spectrograph, built with CaF_2 optics, to provide good transmission and high image quality over the entire nominal wavelength range. A set of user-selectable reflective gratings provides low to medium spectral resolution of approximately 1.5, 3.2, and 7 Å in first order, depending on the groove density (1200, 600, 300 grooves mm^{-1}). While the standard integral field unit (IFU) uses a 16 × 16 element lens array, which provides seeing-limited sampling in a relatively small field of view (FOV) in one of three magnifications (8″ × 8″, 12″ × 12″, or 16″ × 16″), a recently retrofitted bare fiber bundle IFU (PPak: PMAS fiber pack) expands the FOV to a hexagonal area with a footprint of 65″ × 74″. Other special features include a cryogenic CCD camera for field acquisition and guiding, a nod-shuffle mode for beam switching and improved sky background subtraction, and a scanning Fabry-Pérot etalon in combination with the standard IFU (PYTHEAS mode). PMAS was initially designed and built as an experimental traveling instrument with optical interfaces to various telescopes (Calar Alto 3.5 m, ESO VLT, LBT). It is offered as a common-user instrument at Calar Alto under contract to MPIA Heidelberg since 2002.

1. INTRODUCTION

Unlike optional integral field units (IFUs) that can be deployed in front of a conventional slit spectrograph, PMAS (Potsdam Multi-Aperture Spectrophotometer) was designed as a dedicated integral field spectrophotometer. It was built entirely at the Astrophysical Institute of Potsdam (AIP), Germany. Initially designed as a traveling instrument, PMAS was commissioned and subsequently installed as a common-user in-

strument at the Cassegrain focus of the Calar Alto Observatory 3.5 m telescope in southern Spain.

The instrument was specifically designed to address the science case of 3D spectrophotometry of spatially resolved, individual objects, with an emphasis on broad wavelength coverage in the optical wavelength regime. The spectrograph camera was designed to accommodate a single 2K × 4K, 15 μm pixel CCD or a 2 × 2K × 4K mosaic for the full field, providing 2048 or 4096 pixels in the spectral direction and 4096 pixels in the spatial direction, respectively. The standard lens array IFU has a relatively small field of view (FOV) of 16 × 16 square spatial elements ("spaxels") on the sky, corresponding to 8″ × 8″, with seeing-limited sampling of 0″.5 spaxel^{-1}, or 16″ × 16″ in the 2 × magnification mode, with a sampling of 1″.0 spaxel^{-1}. The instrument is based on a modular design, including a telescope module with fore-optics and the

---

standard IFU, a fiber module to couple the light from the IFU to the spectrograph, and the fiber spectrograph with CCD camera. The fore-optics, standard IFU, and spectrograph optics are all built from fused silica, CaF$_2$, or other UV-transparent media such that PMAS is optically corrected and transparent from 0.35 to 1 μm. The instrument also includes a direct-imaging cryogenic CCD camera for field acquisition and guiding.

Since commissioning at Calar Alto in 2001, several new features (facilitated by the open and modular structure of PMAS) have been added to the initial configuration of the instrument: an off-axis fiber bundle (PPak: PMAS fiber pack) for an enlarged FOV > 1′ (Verheijen et al. 2004), a "nod-shuffle" mode of operation for faint-object integral field spectroscopy (Roth et al. 2002d), and the PYTHEAS mode with a scanning Fabry-Pérot etalon for an increased spectral resolution over a large free spectral range (Le Coarer et al. 1995). We will give detailed reports on these special modes in future Papers II, III, and IV, respectively.

The initial conceptual design, progress reports on assembly, integration, and testing, and first results from commissioning are given in Roth et al. (1997, 1998, 2000b, 2000c, 2002a, 2002b, 2002c, 2003) and Kelz et al. (2003a, 2003b). The first results from a science verification run were reported in Roth et al. (2004a).

In this paper, we briefly outline the science drivers for the instrument (§ 2), describe the final design, manufacture, and commissioning (§ 3), and provide information on the performance at the telescope (§ 4).

2. SCIENCE CASE AND REQUIREMENTS

Integral field spectroscopy[4] is an emerging observing technique on the verge of becoming a standard method. After a period of experimental developments since the late 1980s, several facility instruments in the optical and near-infrared (NIR) were planned and subsequently built for some 4–8 m class telescopes; e.g., INTEGRAL at the William Herschel Telescope (Arribas et al. 1998), Gemini's GMOS-IFU (Allington-Smith et al. 2002) and GNIRS-IFU (Elias et al. 1998), and the Very Large Telescope's FLAMES-IFU (Pasquini et al. 2000), VIMOS-IFU (Le Fevre et al. 2003), and SINFONI (Eisenhauer et al. 2003). In this ground-breaking era, PMAS was intended to contribute to the development of "crowded-field 3D spectroscopy," analogous to the successful introduction of "crowded field photometry" with the advent of CCD detectors in astronomy.

Unlike most of the more conventional applications of 3D spectroscopy, in which the simultaneous coverage of a (preferably large) area for the purpose of creating two-dimensional maps of emission-line intensities, velocity fields, velocity dispersions, absorption line indices, etc., have determined the technical requirements (e.g., de Zeeuw et al. 2002), the primary

goal for PMAS was to provide an optimal sampling of the point-spread-function (PSF) over the entire optical wavelength region, from the atmospheric cutoff in the UV to the NIR. Such properties would make an integral field spectrograph an ideal tool for the spectrophotometry of faint point sources, with superior properties over slit spectrographs in terms of slit losses, sensitivity to differential atmospheric refraction and pointing errors, and accurate background subtraction in fields where source confusion is an issue (Roth et al. 1997, 1998, 2000a).

Among the major science cases to demand such properties are spectrophotometry of resolved stellar populations in nearby galaxies (including extragalactic planetary nebulae, H II regions, and optical counterparts of ultraluminous X-ray sources), supernovae, gravitationally lensed QSOs, QSO host galaxies, and high-redshift galaxies. The recent discussion of the science case for extremely large telescopes (ELTs) has shown that this motivation is in fact timely and relevant for future developments in ground-based optical astronomy (e.g., Najita & Strom 2002; Hawarden et al. 2003). We summarize some of the first PMAS results on these topics in § 4.13.

The PMAS requirements derived from these science cases include wide wavelength coverage of 0.35–1 μm, high efficiency, low to medium spectral resolution, seeing-limited spatial sampling over a modest FOV, high stability, a supporting direct imager for field acquisition, guiding, and differential spectrophotometry, and a self-contained design (traveling instrument).

The science case for the bare fiber bundle IFU (PPak) is identical to that of SparsePak (Bershady et al. 2004; see Verheijen et al. 2004). It is complementary to the standard IFU, in the sense that it addresses the problem of low surface brightness 3D spectroscopy using large spaxels over a large FOV at the expense of spatial resolution.

3. INSTRUMENT DESCRIPTION

3.1. Overview

PMAS is based on the principle of a fiber-coupled lens array IFU employing a dedicated fiber spectrograph. Initially, PMAS was required to operate as a traveling instrument. Therefore, the instrument was designed for operation at the Cassegrain focus station of a 4–8 m class telescope with a self-contained structure, having a minimal number of interfaces to its environment. It has a modular layout, with the following major components (Fig. 1, Table 1): a telescope module with flange to the telescope, a main frame as a support structure for the remaining modules, a fiber spectrograph, a fiber module connecting the telescope module and the fiber spectrograph, and an electronics rack for the instrument control subsystem. Except for the telescope flange, the 230 V AC power cable, a connection to the local area network (LAN), and two pairs of cooling hoses for a closed-cycle heat exchanger, PMAS has no connections to the outside world.

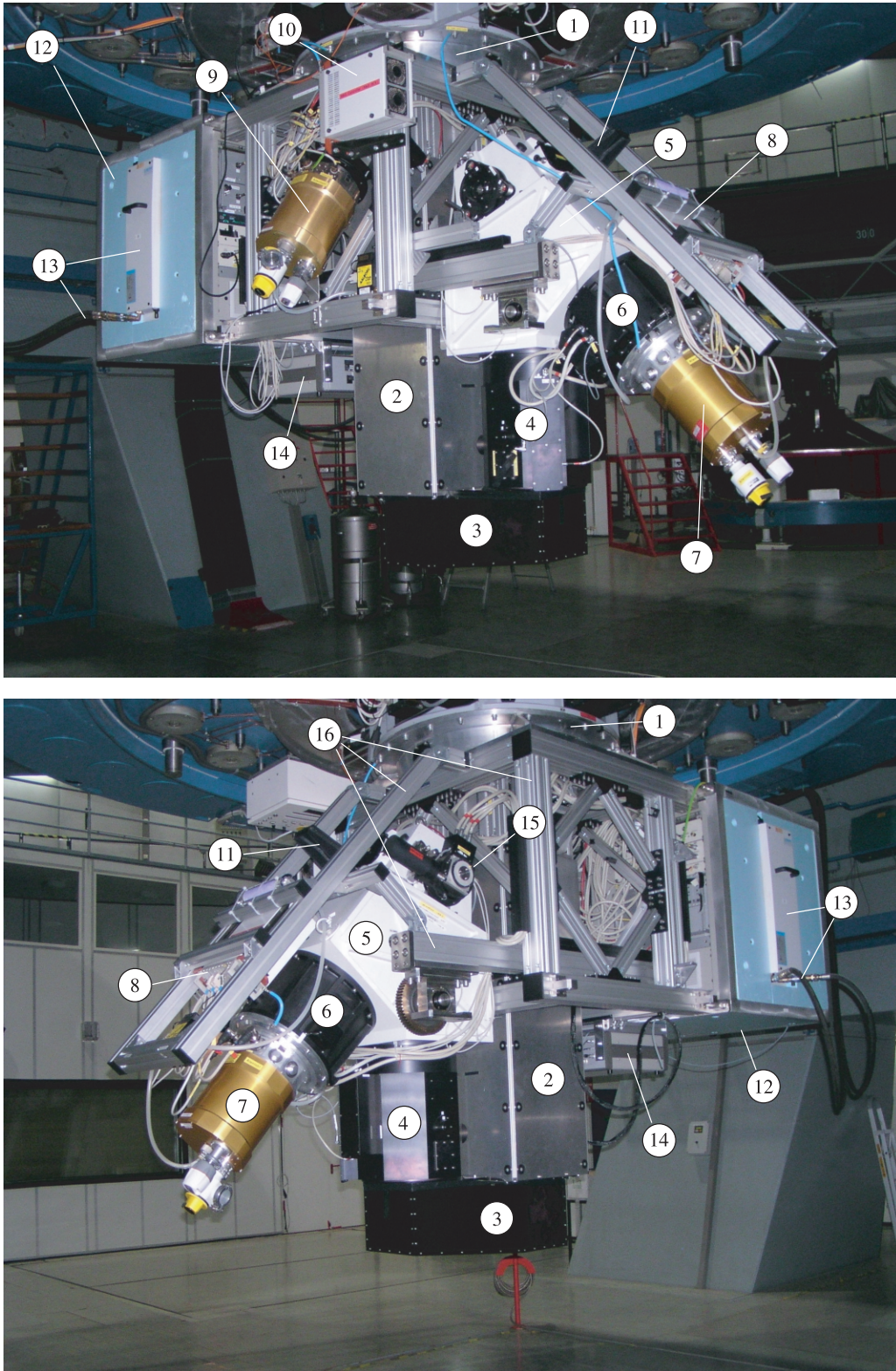
[4] Also referred to as "3D spectroscopy."

Fig. 1.—PMAS at the Calar Alto 3.5 m telescope Cassegrain focus: (1) instrument flange, (2) telescope module, (3) fiber module, (4) spectrograph collimator, (5) spectrograph center case, (6) spectrograph camera, (7) spectrograph CCD, (8) spectrograph CCD controller, (9) A&G CCD, (10) A&G CCD controller, (11) grating platform, (12) electronics, (13) cooling subsystem, (14) Fabry-Pérot controller, (15) grating rotator, (16) main frame. The instrument measures approximately 2 m from the bottom to the telescope flange.

TABLE 1
MAIN INSTRUMENT PARAMETERS

Parameter	Value
Spectrograph	
Focal station	Cassegrain
Principle of operation	IFU+fiber-coupled spectrograph
Spectrograph type	Fully refractive f/3 collimator and f/1.5 camera
Wavelength range	0.35–1.0 μm (CaF$_2$ optics)
Gratings	1200, 600, and 300 groove mm^{-1} reflective gratings
Linear dispersion	Approximately 0.35, 0.8, and 1.7 Å pixel^{-1}
Spectrograph FOV	60 × 60 mm^2
Spectrograph detector	Single 2K × 4K, or 2 × 2K × 4K mosaic CCD camera, 15 μm pixels
Lens Array IFU (LARR)	
Principle of operation	Square lens array with magnifying fore-optics
Lens array	16 × 16 square elements, 1 mm pitch
Fore-optics magnifications	0″.5 sampling, 8″ × 8″ FOV
	0″.7 sampling, 12″ × 12″ FOV
	1″.0 sampling, 16″ × 16″ FOV
Fiber configuration	256 OH-doped fibers, 100 μm core diameter
Filters	Filter slider with five 1 inch round filter positions
Fiber Bundle IFU (PPAK)	
Principle of operation	Focal reducer+hexagonal packed fiber bundle
Fore-optics	Focal reducer lens F/10 to F/3.3, plate scale: 17″.7 mm^{-1}
Fiber configuration	331 object + 36 sky + 15 calibration fibers, 150 μm core diameter
Field of view	74″ × 65″, hexagonal
Spatial sampling	2″.7 per fiber diameter, 3″.45 pitch (nearest neighbor)
Filters	User-selectable 35 × 140 mm^2 order separating filter in spectrograph collimator mount; alternatively, 50 mm round filter in front of fiber bundle
Acquisition and Guiding Camera	
Detector	1K × 1K CCD, thinned back-side illuminated, AR coated
Field of view	205″ × 205″
Pixel size, scale	24 μm, 0″.2 pixel^{-1}
Filters	Filter slider with four 2 inch round filter positions

3.2. The Spectrograph Module

In terms of importance and costs, the fiber spectrograph is the dominant component of the instrument and determines to a large extent its overall properties. It employs an all-refractive optical design with an f/3 collimator, a beam size of 150 mm diameter, interchangeable reflective gratings, and an f/1.5 camera with a corrected focal plane of 60 × 60 mm^2. The nominal wavelength range is 0.35–1 μm.

The principal optical design and optimization was performed by U. L. with proprietary software (Laux 1999). The result was double-checked using the commercial ZEMAX and Code V programs. The collimator and camera systems are characterized by a similar layout (see Fig. 2), each consisting of a combination of two lens groups (triplet, quadruplet), combined with two singlet field lenses near the fiber slit (collimator) and the detector focal plane (camera). The camera has two aspherical surfaces, viz., the first surface of the triplet (lens 14) and the first surface of the field lens (lens 18), as seen from the grating. The camera field lens is followed by a plane-parallel quartz plate acting as the cryostat window of the CCD detector

subsystem. The external focus of the camera has the significant advantage of allowing for an easy interchange of detectors.

As a result of the compact configuration of the two front lens groups, the optical system presents comparatively few (18) glass-air interfaces, which are all covered with high-quality broadband AR coatings, yielding an average residual reflectance of 0.8% per surface in the wavelength interval 0.35–1 μm. Due to the excellent transmission properties of the glasses, the system has a high throughput down to 350 nm. The image quality is well matched to the nominal pixel size of 15 μm (Table 4). There is a modest amount of vignetting (≈25%) near the edge of the spectrograph FOV. The masses of the complete collimator and camera subsystems, including the massive lens mounts, are 60 kg each. The optical systems were manufactured and assembled by Carl Zeiss, Jena, Germany. The results of the acceptance tests were reported by Roth et al. (2000b).

The spectrograph's mechanical design is characterized by a solid cast-aluminum housing, which keeps the heavy collimator and camera optics in place. Both lens barrels are protected by
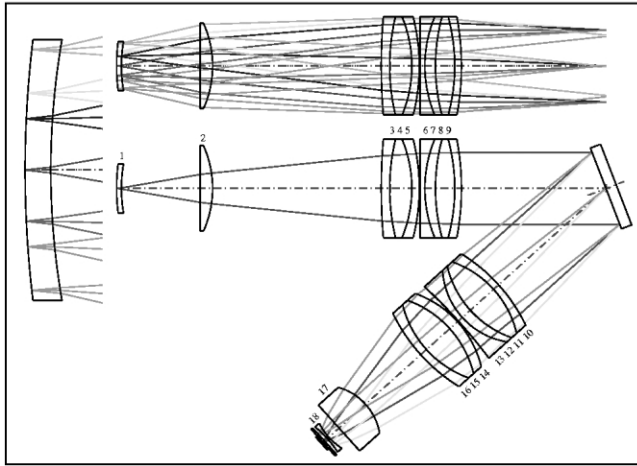
FIG. 2.—*Bottom*: Cross-section of the fiber spectrograph optical system in the plane of dispersion. *Top*: Collimator cross-section, perpendicular to the dispersion. *Left*: Magnified detail of the fiber coupling lens (from the collimator graph at the top). The lens materials are as follows: quartz (lens 1, 2, and 17), CaF$_2$ (lens 4, 8, 11, and 15), BaK4 (lens 3, 5, 7, 9, 10, 12, 14, 16, and 18), and LF5 (lens 6 and 13). The last element in the optical train is the plane-parallel quartz window of the CCD cryostat.

TABLE 2
PMAS Grating Parameters

Grating (1)	ID (2)	Groove Density (3)	D (4)	α_{blaze} (5)	λ_{blaze} (6)	$\Delta\lambda$ (7)
U1200	1	1200	0.39	10.4	300	794
V1200	2	1200	0.35	17.5	500	725
R1200	3	1200	0.30	26.7	750	609
I1200	4	1200	0.22	36.8	1000	460
J1200	5	1200	0.22	46.0	1200	450
J1200[a]	5	1200	0.17	46.0	600	341
U600	6	600	0.81	5.2	300	1656
V600	7	600	0.80	8.6	500	1630
R600	8	600	0.75	13.9	800	1533
U300	9	300	1.67	2.5	300	3404
V300	10	300	1.67	4.3	500	3404

NOTE.—Col. (1): name; col. (2): identifier; col. (3): groove density (grooves mm^{-1}); col. (4): reciprocal dispersion (Å pixel^{-1}); col. (5): blaze angle; col. (6): blaze wavelength (nm); col. (7): wavelength coverage for 2K × 4K CCD (Å).

[a] Second-order backward.

stiff aluminum tubes mounted to the center case but decoupled from the lenses. The camera tube carries the spectrograph CCD camera, which is also mechanically decoupled from the optics. The design was optimized for high mechanical stability using the ANSYS finite element code (Dionies 1998). The whole spectrograph subsystem is suspended at two points near the center of gravity and mounted to the main frame to avoid the variation of torque over different pointings of the telescope.

The exchangeable reflective grating is mounted on a 360° rotator, which accommodates any required grating orientation, depending on the choice of ruling and blaze. The gratings are fixed in a six-point kinematic mount, the blazed front surface coinciding with the rotation axis of the device. The grating rotator is balanced by counterweights, again to avoid any torque effects under varying orientations.

PMAS is equipped with a set of interchangeable reflective gratings (Table 2), each of which is mounted in an individual frame and stored in a protective cartridge when not installed in the instrument. The gratings were manufactured by Richardson Grating Laboratory, Rochester, New York, as replicas from master gratings for astronomical use, with a ruled area of 154 × 206 mm^2 and a blank size of 165 × 220 × 35 mm^3. Each grating frame carries a 4 bit code made out of small magnets (grating ID), which is read when loading a grating from its cartridge into the grating rotator and is used to generate a corresponding FITS header entry GRAT_ID for each spectrograph data file.

The spectral resolution depends on the choice of grating, the zeroth order projected fiber size on the grating (4 or 6 pixel diameter for the lens array and PPak IFUs, respectively), an-

amorphic (de)magnification (Schweizer 1979), and tilt and orientation of the grating. Depending on the orientation, i.e., the normal of the blaze surface facing either the camera ("forward"), or the collimator ("backward"), the anamorphism is effected in opposite ways, and the tilt must be adjusted accordingly. The grating cartridges are built to allow operation either in forward or backward blaze, with just a minor mechanical modification at the frame. The default orientation of PMAS gratings for spectrophotometry is forward. However, a significant increase in spectral resolution is obtained for the J1200 grating in second-order backward blaze, as discussed in Paper II. A comprehensive listing of grating parameters as a function of grating angle and orientation is given in the PMAS online manual.[5]

3.3. Telescope Module

The telescope module is designed for three major purposes: to reimage the telescope focal plane onto the lens array (fore-optics), to illuminate the lens array from an internal calibration light source (calibration unit), and to project an area around the IFU onto a camera for target acquisition and guiding (A&G subsystem). For the latter, either an external slit-viewing TV guider camera can be used, or alternatively, a cryogenic CCD camera that is internal to the PMAS instrument.

The three optical systems are shown schematically in Figure 3. Light entering from the telescope is combined in the focal plane (FP; intersection of the tilted A&G pick-off mirror and optical axis, upper part of the drawing).

The optical train of the fore-optics begins at a central hole in the pick-off mirror, which gives way for the FOV of the lens array, onto which the telescope focal plane is imaged with a magnification of 1 : 11.8 (for the standard sampling of 0″5

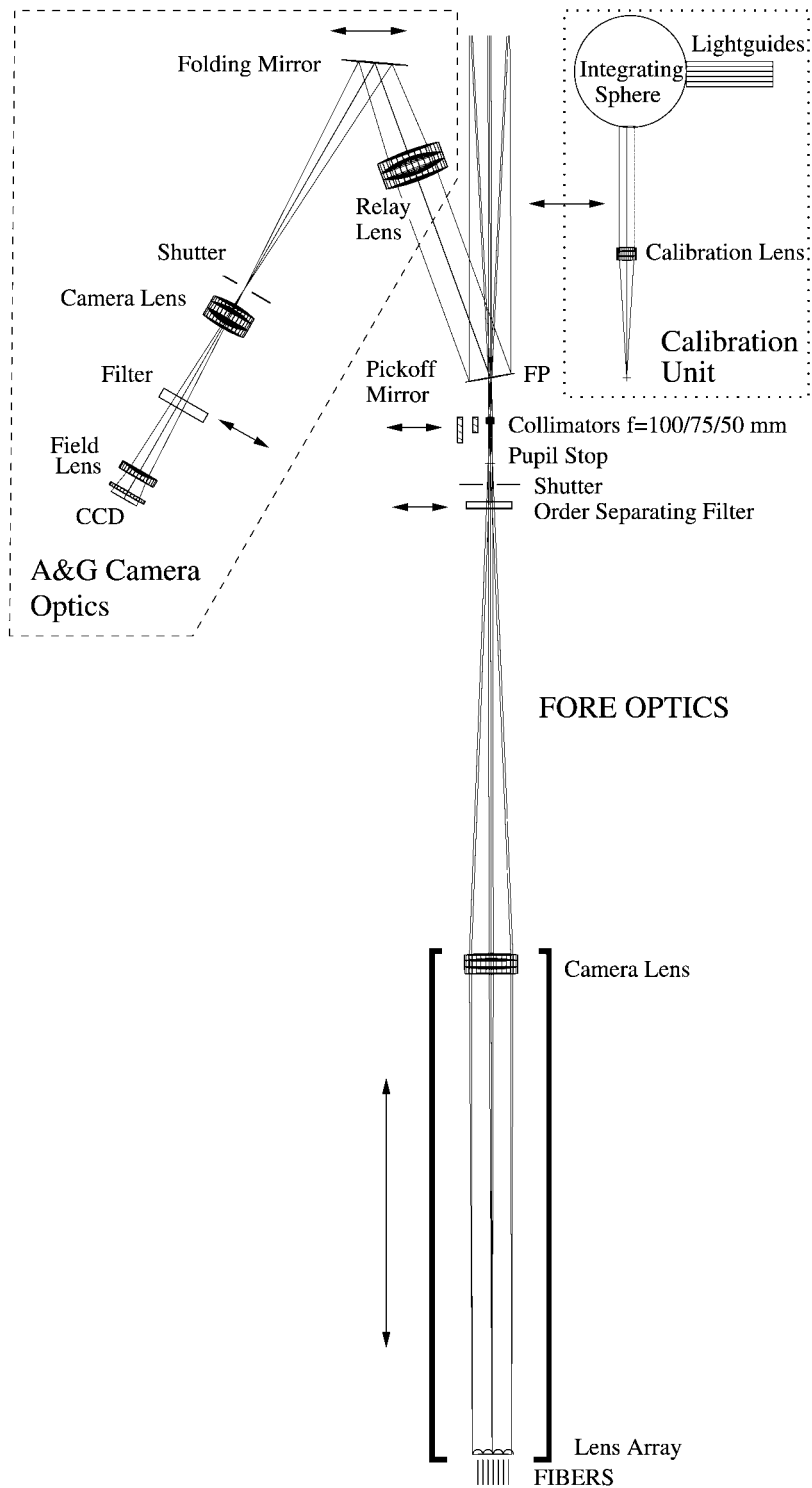[5] See http://www.aip.de/groups/opti/pmas/OptI_pmas.html.

FIG. 3.—Cross-section of the three optical systems of the PMAS telescope module: fore-optics, calibration unit, and A&G camera system.

TABLE 3
FORE-OPTICS PARAMETERS

f'_{Coll} (mm) (1)	Γ (2)	IP (mm) (3)	μP (μm) (4)	Pitch (arcsec) (5)
Calar Alto RCC 3500/35000, f/10				
50.0	700.0	5.00	42.6	0.50
75.0	466.7	7.50	63.8	0.75
100.0	350.0	10.00	85.1	1.00
VLT 8115/108825, f/13.4				
50.0	2176.5	3.73	31.7	0.16
75.0	1451.0	5.59	47.6	0.24
100.0	1088.3	7.46	63.5	0.32
LBT 8408/123765, f/14.7				
50.0	2475.3	3.40	28.9	0.14
75.0	1650.2	5.10	43.4	0.21
100.0	1237.6	6.79	57.8	0.28

NOTE.—Col. (1): collimator focal length; col. (2): intermediate pupil de-magnification factor Γ; col. (3): diameter of intermediate pupil; col. (4): nominal diameter of micropupil (fiber input); col. (5): projected lens array pitch on the sky.

per lens). Reimaging is accomplished through the combination of a collimating lens and a camera objective. Owing to a double 2 × f arrangement of these lenses, an intermediate pupil is formed at the conjugate of the telescope focal plane. For unbaffled telescopes, this is a convenient location for a Lyot stop. Near the intermediate pupil, there is also a shutter and a linear stage accommodating filters of up to 5 orders of separation. The double 2 × f scheme has the disadvantage of a relatively long optical train (≈1 m), but the significant advantage of allowing for future experimental upgrades (e.g., Fabry-Pérot etalon [PHYTEAS mode; Le Coarer et al. 1995; see Paper IV]) or polarimetry. Also, telecentricity for optimal lens array–fiber coupling is ensured without the need for an additional field lens in front of the IFU. Three different magnifications are chosen by interchangeable collimator lenses that are mounted on a linear stage. Table 3 lists the parameters for lenses with focal lengths of 50, 75, and 100 mm, which were computed for three telescopes (Calar Alto 3.5 m, VLT, and LBT f/15 Gregorian focus). Switching to another scale also requires us to adjust the position of the following camera lens and the lens array along the optical axis of the fore-optics. They are mounted at the ends of a stable tube, thus forming a single unit whose position along the optical axis can be adjusted by translation on a precision linear stage.

The calibration unit consists of an integrating sphere whose exit port is imaged onto the intermediate pupil through the calibration lens and the fore-optics collimator, imitating as closely as possible the telescope beam. The correct f-ratio is defined by the calibration lens, while the telescope pupil is mimicked with a stop at the output of the integrating sphere, including a central obscuration to simulate the M2 shadow. The
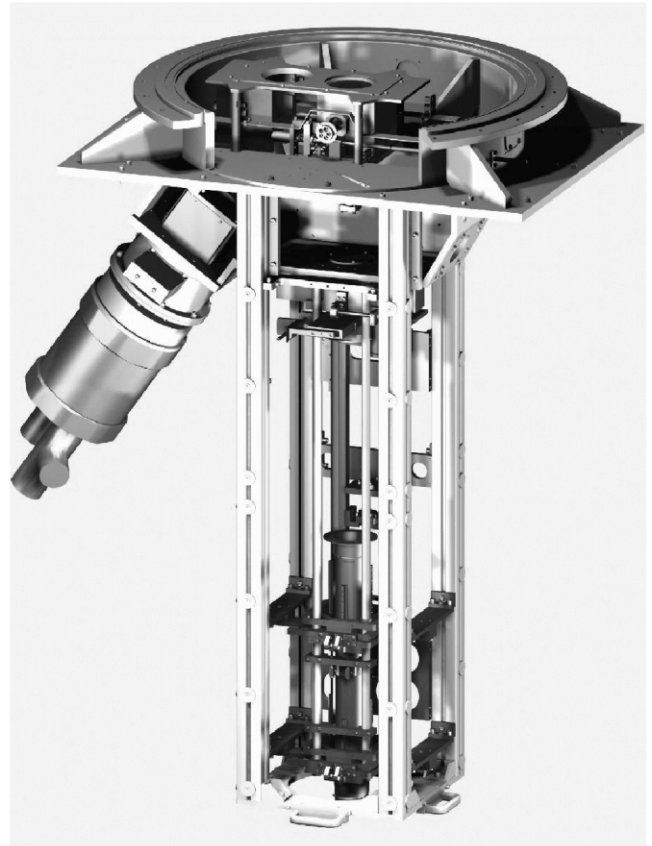

FIG. 4.—Mechanical layout of the telescope module, shown without cover plates (CAD drawing). The cutaway view of the telescope flange provides insight into the linear stage with the calibration unit and A&G camera subsystem devices.

calibration unit is mounted on a linear stage and is moved into the beam for calibration exposures.

The A&G camera subsystem is similar to a conventional slit-viewing system in which the reflective front side of a spectrograph slit is observed with a TV guiding camera. In the case of PMAS, the slit is replaced by the tilted pick-off mirror. The combination of a relay lens, a folding mirror, a camera lens, and a field lens projects the plane of the pick-off mirror onto a CCD, which is used for target acquisition and offset guiding. A filter-stage mechanism accommodates up to four 50 mm filters at a location roughly halfway between the camera and the field lens.

Mechanically, the telescope module consists of a rigid cast-aluminum housing with a flange to the telescope, which also forms the base for the support frame, and a tower-like structure extending from the flange down to the fiber module (Fig. 4). The tower acts as a stable mechanical support for the optical bench, which is carrying the entire fore-optics system. It is essentially self-contained and can be dismounted for shipping as a whole subsystem. The optical bench consists of LINOS Macrobench elements and custom-made components for the
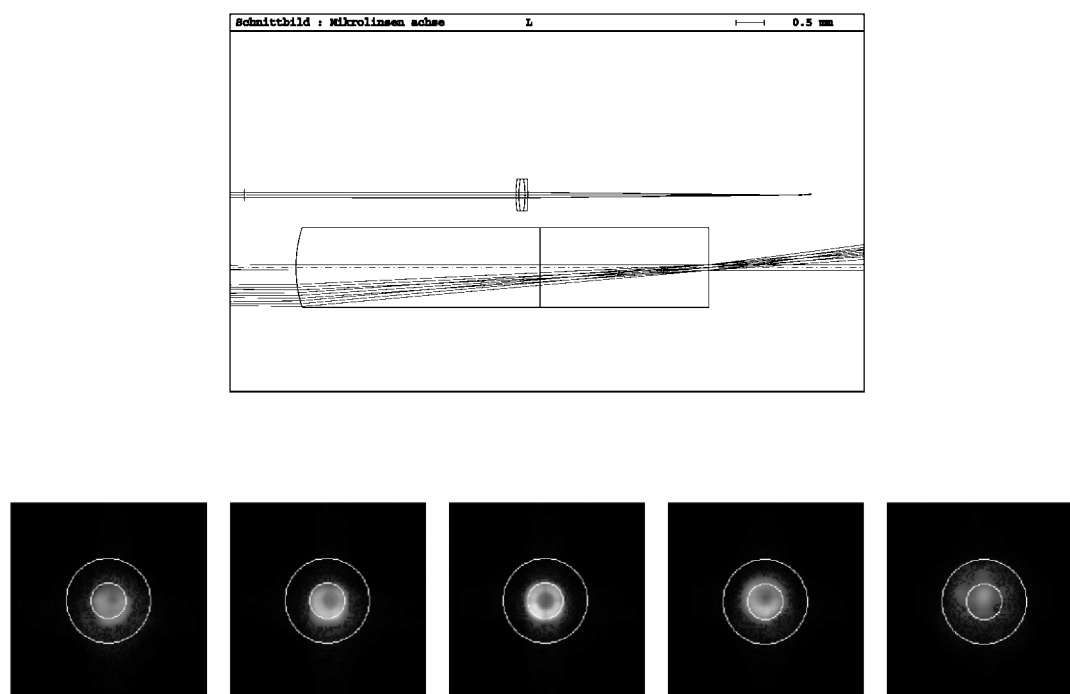
Fig. 5.—Lens array pupil imagery. *Upper panel*: Cross-section of lens array with fore-optics (*top*: pupil-camera lens-lens array; *bottom*: magnified view of a single lenslet). *Lower panel*: Through-focus series of micropupil image at the back side of the lens array, observed with microscope+CCD imager in the lab. The sharp, in-focus frame (*middle*) shows the telescope pupil with M2 shadow and spider, created with telescope simulator optics; *inner circle*: nominal micropupil diameter (43 μm); *outer circle*: fiber core diameter (100 μm).

movable parts, namely the linear stages for the collimator lenses, order-separating filters, and the camera–lens array tube.

The calibration unit on its linear stage is visible in Figure 4 through the cutaway view of the flange. An input piece provides a port for six waveguides to simultaneously feed light from remote light sources (continuum and spectral line lamps) into the integrating sphere.

The A&G camera is the prominent LN$_2$ Dewar seen in the left-hand side of Figure 4, attached to the telescope module housing at an angle. Its flange, together with another macro-bench assembly, forms a modular subsystem that carries all the optomechanical elements and can be easily removed from the housing for inspection and maintenance. The cap of the filter stage, which itself is yet another modular subsystem, is visible as a rectangular structure at the front part of the detector flange.

3.4. Integral Field Units

3.4.1. Lens Array IFU (LARR)

The main PMAS IFU for performing spatially resolved spectrophotometry is the lens array, mounted at the end of the fore-optics optical train (Fig. 5). The open modular design allows another device to be exchanged without necessarily having to modify other major subsystems. The current lens array is a monolithic 16 × 16 element, 1 mm pitch square array with square lenslets made from fused silica. It was manufactured by

Advanced Microoptic Systems GmbH, Saarbrücken, Germany, as a custom-designed element with aspherical lenslet front surfaces and a common-plane back side where the fiber bundle is attached (Roth et al. 2000c). The optimal surface quality derived from an interferometric acceptance test was measured to 50 nm rms, excluding a strip ~10 μm wide at the four intersections of a surface with its four nearest neighbors. Owing to the aspherical surface, the lens is in principle free of spherical aberrations. However, due to random surface defects and an edge effect at the borders of a lenslet, which cannot be made arbitrarily sharp, the overall real image quality is less than ideal (see § 4.3). The output F-number is 4.5. Details of the coupling of the lens array to the fiber bundle are described in § 3.5.

3.4.2. Bare Fiber Bundle IFU (PPak)

In addition to the standard IFU using the on-axis lens array, PMAS was equipped with a second IFU in 2004. This IFU consists of a bare fiber bundle (called PPak), which is placed approximately 6′ off-axis so as not to obstruct the field for the lens array or the A&G camera. The main purpose of PPak is (1) to provide a wide FOV and (2) high light-collecting power per spectra, rather than contiguous spatial sampling. A focal reducer lens is placed immediately in front of the fiber bundle to reduce the telescope beam from F/10 to F/3 and to change the telescope plate scale from 5″9 to 17″8 mm^{-1}. Altogether,

the PPak bundle features 382 fibers, of which 331 are placed in a densest packed hexagonal array that projects to $74'' \times 65''$ on the sky. Thirty-six sky fibers are arranged within six surrounding mini-IFUs located $72''$ away from the central object fiber. Finally, 15 fibers are diverted from the IFU and can be illuminated by calibration lamps to provide simultaneous calibration spectra within the science exposures.

The combination of $2\rlap{.}''7$ fibers and the high efficiency and wavelength coverage of the PMAS spectrograph makes PPak a unique tool to study extended low surface brightness objects, which require high light-collecting power and a large FOV. A more detailed description is given in Paper II and Kelz et al. (2004).

3.5. Fiber Module

The purpose of the fiber module is to rearrange the two-dimensional information sampled by the IFU onto a linear pseudoslit. Additionally, the fibers decouple the IFU and fore-optics from the spectrograph, so that any mechanical flexure within the telescope module is not transferred to the spectrograph, and seeing effects do not change the spectral resolution (i.e., the slit width).

PMAS is used for the spectroscopy of crowded fields and of faint, background-limited objects. For these targets, poor flat-field calibration is a major limitation to the extraction of reliable spectrophotometry. PMAS features a novel design of exchangeable fiber arrays. Instead of permanently bound fibers, both ends of the PMAS fibers are mechanically aligned and optically matched to lenses in such a way that fibers can be replaced. The effect of this setup is twofold. First, this allows any fibers that perform below average to be replaced until the overall efficiency is maximized and discrepancies between individual spectra are minimized. Second, this makes it possible to maintain the performance of the fiber unit during its lifetime, as any damaged or broken fibers can be replaced without the need of building a completely new IFU. While this adds certain complications to the manufacturing process (small mechanical devices, potential damage of the fiber end faces during assembly, imperfections of the index matching, and alignment), these can be addressed by strict quality control. The aim of the PMAS fiber module is to achieve high efficiency while ensuring a photometrically stable flat-field characteristic over time.

As PMAS was specified to be a medium-resolution spectrophotometer, it was decided that a bench-mounted remote spectrograph with long fiber lengths should be avoided, since it would be subject to movement and create modal noise (Schmoll et al. 2003). Instead, PMAS features fiber lengths of approximately 2 m. This ensures that the internal attenuation of the fibers is low (~98%), while the input modes are still sufficiently scrambled.

The fiber module consists of three subunits: the integral field section, the fiber loop box, and the fiber slit. There is no stiff mechanical connection between them, therefore no flexure can

be transmitted from one end to the other. Both the individual units and the overall assembly are fully enclosed by a cover for the purpose of mechanical protection and light tightness (see Fig. 6).

The fibers chosen are type FVP100120140 from Polymicro, Inc., since the core size, FRD (focal ratio degradation) performance, and spectral attenuation were found to best fit the PMAS requirements. These step-index silica fibers are OH enhanced, have a core diameter of 100 μm, a clad/core ratio of 1.2, and a numerical aperture of 0.22. The fibers are inserted into a three-layer PVC-Kevlar tubing (from Northern Lights Cable, US) for protection and fitted with end connectors for mounting purposes.

At the output end, the bare fibers are glued onto small blocks, called slitlets, that once assembled form the fiber slit. At the input end, the fibers are held by thin metal sheets, called fieldlets, that are stacked on top of each other to form the two-dimensional integral field at the back side of the lens array.

The fiber module contains 256 fibers arranged in groups of 16. The fiber arrays are self-contained elements that can be mounted and demounted from end to end within the fiber module for the purpose of repair or replacement. Additionally, it is also possible to remove the entire fiber module from the PMAS instrument and replace it with an updated or modified version. Both the lens array at the fiber input and the first spectrograph lens at the fiber output are optically matched to the fibers, using optical gel (code 0608 from Cargille Laboratories). The effect of index matching the fiber ends is twofold. First, reflection losses at glass-to-air interfaces are reduced, and second, some imperfections of the fiber-end surfaces are cured by the gel. Tests done by Schmoll et al. (2003) and by Kelz et al. (2003b) demonstrate that fibers that are index-matched to a glass plate or a lens array show an increase in flux transmission of approximately 10% and a reduced fiber-to-fiber variation.

The current PMAS lens array of 16×16 elements forms 256 micropupils with diameters of 43 to 85 μm (see Table 3) simultaneously, which need to be imaged onto 100 μm fibers each. The common mount that holds the lens array and the fiber ends ensures that all fibers are placed at the correct lateral and focal position with respect to the micropupils, to within ± 5 μm (see Fig. 7).

Instead of a permanently bound structure, the solution for PMAS consists of a mechanical mount that holds both the lens array and the fiber arrays. A position mask is situated 0.2 mm behind the back side of the lens array. The position mask consists of 256 holes with inner diameters of 150 ± 3 μm and a pitch of 1 ± 0.003 mm. The mount provides a frame with grooves spaced 1 mm apart, into which the fieldlets, carrying the fibers, can be inserted and secured. The fieldlets are manufactured in such a way that once they are inserted in the mount, the fiber ends are located at the micropupil plane (back side) of the lens array. While the fiber assemblies and the mask are fixed in position, it is possible to translate and rotate the lens
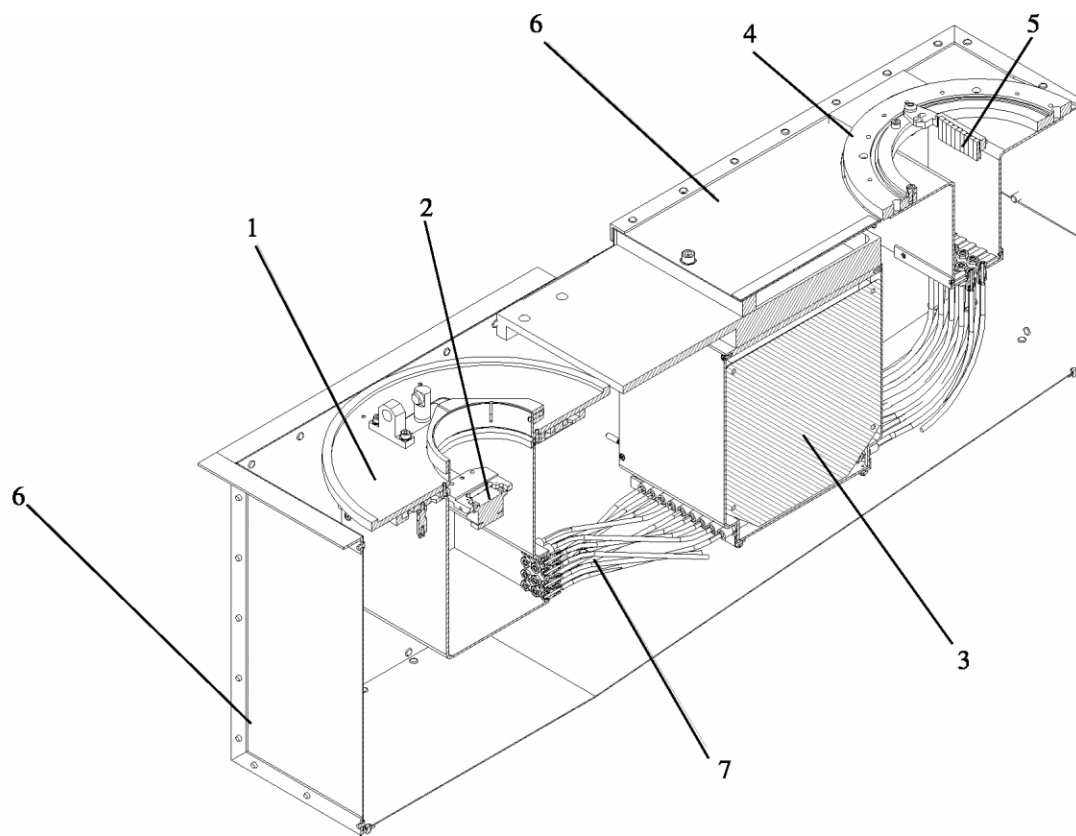
FIG. 6.—Cutaway view of the PMAS fiber module with components: (1) IFU holder, (2) lens array, (3) fiber loop box, (4) fiber slit, (5) slitlets, (6) fiber module cover, (7) fiber tubing. (Not shown are the 256 individual fibers.)

array, using three micrometer screws, for the purpose of alignment.

The lens array mount can be equipped with one of four calibration masks to cover vertical strips of the lens array (see Fig. 8). As a result, only every second, fourth, or 16th fiber of the pseudoslit is illuminated, allowing one to measure the faint extended wings of the spectral profiles in the cross-dispersion direction. The actual *measurement* of the profile is a method of accurately modeling the spectra for optimal extraction techniques, the correction of cross talk, and the determination of an instrumental stray light model (see § 3.8).

It is essential to mount fibers without inducing stress caused by pressure, pulling, or strong bending, which otherwise increases the FRD and affects the performance. To avoid any stress, the fibers are inserted in protective tubing, ensuring only moderate bending radii. Additionally, the fiber module features a box for surplus fiber loops to avoid fiber breakage and to provide a reservoir of extra cable as needed during assembly and adjustments of the fore-optics focal length.

The output ends of the fibers are assembled onto 16 blocks (slitlets) and arranged side-by-side to form a 96 mm wide array (the fiber slit; see Fig. 9). The spacing from fiber to fiber is 0.34 mm (= 3.4 fiber core diameters), resulting in a spectra-

to-spectra distance, that is sufficient to perform an interlacing nod-and-shuffle (beam-switching) mode (Roth et al. 2004d; see also Paper III). The fiber slit can accommodate double the number of fibers (512) at half the spacing (corresponding to 7 pixels at the detector). The spectrograph F/3 collimator accepts the whole fiber output cone, without the need of additional beam-converting microlenses. The optical design of the spectrograph requires a curved fiber slit that directly couples to the surface of the first collimator lens, with optical gel matching the refractive indices.

3.6. The Detector Subsystems

PMAS is equipped with two cryogenic CCD systems: one for the spectrograph camera, and another one for the A&G camera. Except for some detector-head and cable details, both subsystems share the same layout based on ESO designs that were copied and adapted with permission. The CCD subsystems each consist of a commercial Infrared Laboratories ND8 cryostat, a detector head with detector-head electronics, cables, and a CCD controller. The spectrograph detector head was built according to the VLT design as described by Lizon (1997), whereas the A&G camera detector head was made on the basis
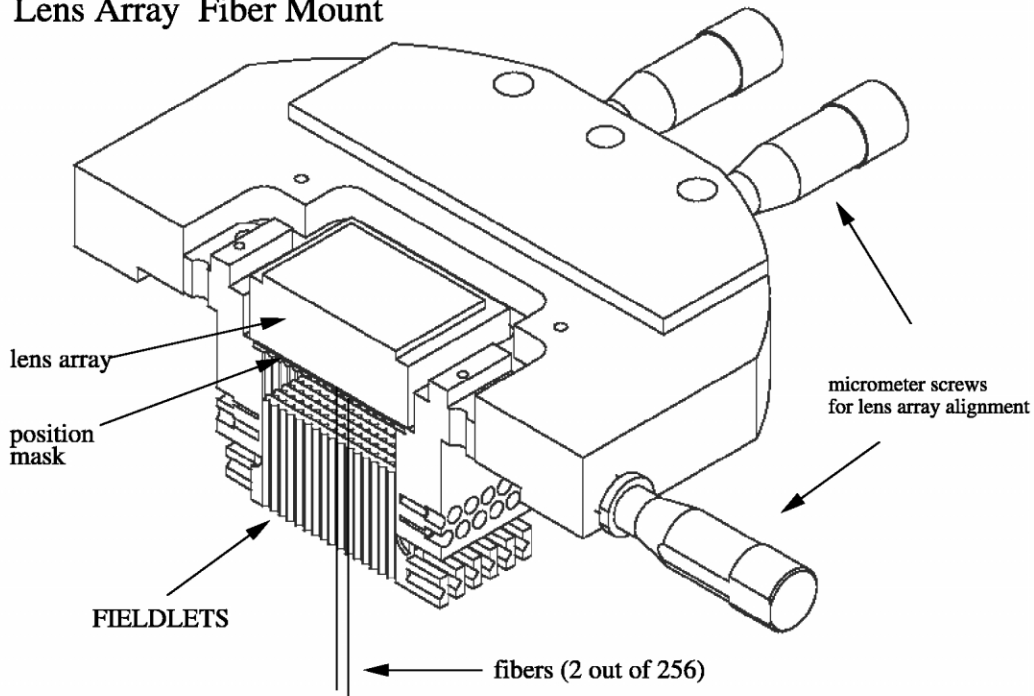
FIG. 7.—Cutaway view of the lens array mount, illustrating how the fieldlets with the fibers are positioned behind the adjustable monolithic lens array.

of an earlier design for La Silla, which was also used for the MONICA instrument (Roth 1990). The CCD controllers are modified copies of ACE (ESO Array Control Electronics), which was originally developed by Reiss (1994) for the ESO VLT technical camera systems. ACE is based on a transputer-DSP architecture employing the (now discontinued) INMOS T805/T225 transputer chips and a Motorola 56001 DSP. Both controllers are connected via transputer links to an onboard UltraSPARC station via SBUS interface cards. The SPARC supervises the ACEs and handles CCD requests and the associated image data streams.

The CCD software is a client-server–based application written by T. F. The original INMOS server program was enhanced with an EPICS interface layer (see § 3.7), providing all necessary control functions, such as initialization, wipe, dark/bias/real exposures, window readout, binning, etc., from UNIX shell scripts. Shutter control is also performed from this environment. A most useful feature of the CCD software is that each
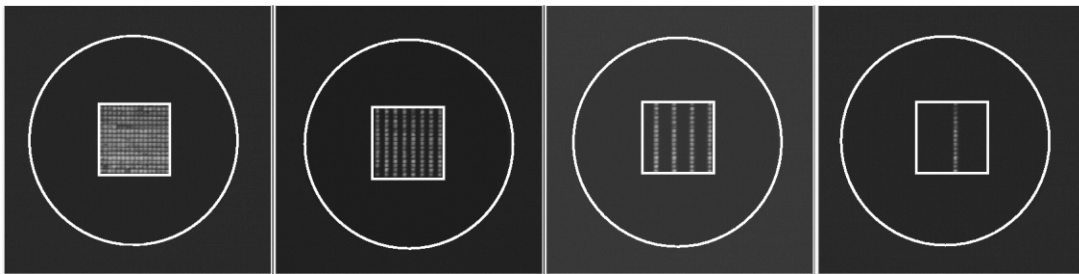

FIG. 8.—Snapshots of the (backwards illuminated) PMAS lens array. Calibration mask stops can be inserted in front of the lens array to partly block the IFU for calibration purposes (see text). *Left to right*: Full FOV of 16 × 16 elements, every second column blocked, every fourth column open, only one column (i.e., every 16th spectrum illuminated).
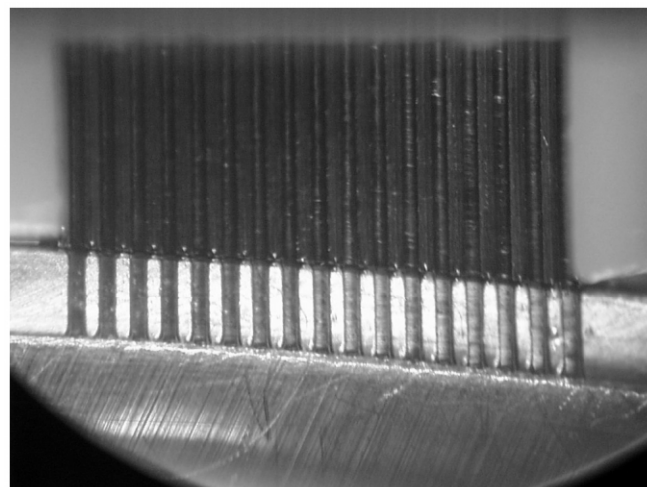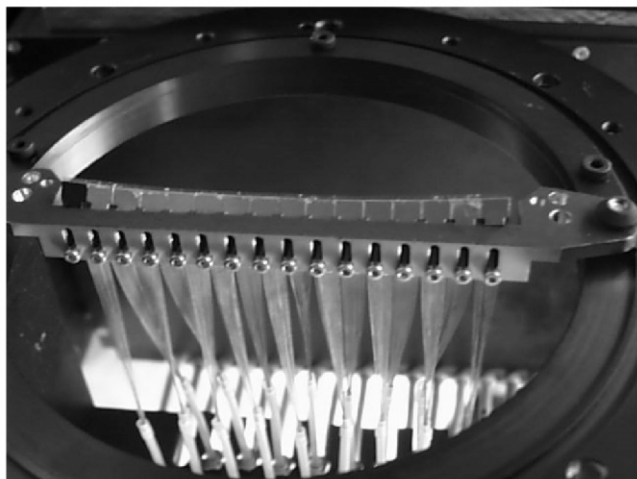
Fig. 9.—*Left*: Photo of the assembled fiber slit, which consists of 16 blocks with 16 fibers each, yielding 256 fibers in total. *Right*: Detailed view of a single slitlet. Note the accurate position of the fiber end faces, the overall curvature of the slit, and a 17 th spare fiber per block.

relevant ACE hardware and software parameter is reflected (and updated) in the EPICS real-time database, providing seamless access from high-level software and advanced scripting without requiring any low-level software updates or modifications. The PMAS nod-shuffle mode (described in Paper III) makes particular use of this scheme of low-level scripts and database parameters.

PMAS is currently equipped with three fully functional cryostat/detector-head subsystems and five ACE controllers (three of which are spare units). There is one cryostat/detector head for the A&G camera system, with a thinned $1K \times 1K$ SITe TK1024 chip and a pixel size of 24 μm that is matched to the optical system to yield a plate scale of $0\farcs2$ pixel^{-1}. The A&G camera FOV is $3\farcm4 \times 3\farcm4$. The two remaining cryostats have alternative CCD configurations with (1) a single SITe ST002A $2K \times 4K$ chip, pixel size 15 μm square, and (2) a mosaic of two such chips covering the whole useful focal plane of the spectrograph camera of $4K \times 4K$ 15 μm pixels. Owing to the external focus of the spectrograph optics, interchanging CCD cameras 1 and 2 is a rather simple mechanical operation.

3.7. Instrument Control

3.7.1. Instrument Control Electronics

Except for the exchange of gratings and filters, PMAS is operated under remote control, without direct human interaction at the instrument. The instrument control electronics was designed as a self-contained subsystem and was built into a dual 19 inch electronics rack. It is mounted in a rigid custom-designed aluminum frame, which in turn is suspended in the main frame. It contains the following major components: a VMEbus computer as master hardware controller, a SPARC workstation for data acquisition and high-level instrument control software, DC and stepping motor controllers, motor power amplifiers, a

shutter controller, a calibration unit with six shutter-controlled continuum and spectral-line lamps, various power supplies, and miscellaneous support and auxiliary electronic units. The substantial amount of dissipated heat (typically 600 W) is removed through eight front-panel–mounted fans when the instrument is operated off telescope, or by means of two liquid-cooled heat exchangers during observations at the telescope. The VME subsystem contains various boards for dedicated control functions: single-board computer MVME167 (VME master) running under the real-time operating system VxWorks, PMAC motor controller for up to eight drives, accompanied by a 64 channel digital input/output board for general purpose I/O (sensing switches, controlling lamps and shutters), MAC4-STP stepper motor controller for four stepping motors, and a temperature monitor board for RTD (resistance temperature detector) sensors.

The following motorized functions are served by the electronics subsystem: focus of the spectrograph collimator and camera, grating rotator, focus of the A&G camera optical system, filter exchange stage of the A&G camera, linear stage for the exchange of fore-optics collimator lenses (changing the IFU scale/magnification), linear stage to adjust fore-optics for the difference in focal length of different collimators, fore-optics exchange mechanism for different order-separating filters, linear stage to deploy/retract the calibration unit into/from the telescope beam, and linear stage to insert the relay optics of the A&G camera. In addition to these motor-controlled functions, there are six individually controlled mechanical shutters for the lamp modules of the calibration unit, the fore-optics shutter, and the spectrograph slit shutter, which resides inside of the spectrograph collimator. The linear-stage motors are protected against malfunction through a variety of redundant inner- and outer-limit switch pairs, as well as fail-safe interlock

schemes for those drives that are subject to potential collision states. All motors are equipped with gears, precision linear or circular position encoders, and tacho encoders. The grating rotator, which yields a positioning accuracy of 5″, is equipped with a DC motor coupled to a HarmonicDrive gear and followed by a precision rotator stage, both of which are designed to exhibit zero backlash.

The VMEbus computer, the SPARC workstation, and an associated terminal server are connected via ethernet and a layer-three switch to the LAN. The terminal server offers console access to each computer and the PMAC motor controller, which allows us to start up the instrument and boot the computers from a remote login, as well as provide direct access for diagnostics purposes.

3.7.2. Instrument Control Software

The PMAS instrument control software has a hierarchical structure (Fig. 10), which is implemented on two main computers (target/host) and a number of embedded controllers. The host system is a UNIX workstation running EPICS (Experimental Physics and Industrial Control System[6]). The target system is a VMEbus single-board computer running under the real-time operating system VxWorks. The Input/Output Controller (IOC) part of EPICS is implemented on the target.

The low-level target software consists of a state program and the EPICS real-time database accompanied by hardware drivers and PLC and motion programs running on the PMAC motor controller. The EPICS database is a graphically designed software entity that, once booted, runs continuously, similar to a common hardware device. Instrument control and logging functions are triggered periodically or are driven by events or interrupts. A useful feature of the EPICS real-time database is the availability of each instrumental parameter known to the instrument control software. Host controllers and IOCs communicate via LAN. EPICS offers a communication mechanism called Channel Access, providing transparent network access from host controllers and IOCs to EPICS database process variables just by name.

The low-level software is broken down into CCD-related tasks (CCD controller) and other hardware-related tasks (VME controller), both of which are coordinated and monitored by the EPICS database. From the user point of view, all low-level tasks are accessible from a UNIX command-line interface with a variety of low-level shell scripts. In addition, a generic EPICS graphical user interface (GUI) provides status information about all major mechanical devices, lamps, and other parameters such as temperature, CCD cryostat evaporating N_2 flow rates, etc. (PMAS status window).

A second-level command-line interface is provided through a collection of IDL scripts that interface to the low-level software and EPICS database and relieve the user from the detailed

knowledge of device parameters. All basic instrument control functions like starting CCD exposures, switching lamps on/off, setting the grating, focus, and so forth are accessible through these comprehensive scripts, which also include basic help features, as well as logging and diagnostic functions. Elementary scripts can be easily combined to form more complex macros for complete measurement cycles, including the evaluation and visualization of results.

On top of the PICS command-line interface, two major GUIs (also written in IDL) are available for observing at the telescope: the spectrograph CCD control interface and a corresponding tool for the A&G camera.

3.8. Data-Reduction Software

Based on experience gained with the Multipupil Fiber Spectrograph (MPFS) instrument at the 6 m Bolshoi Teleskop Azimutal'nij in Selentchuk (Si'lchenko & Afanasiev 2000), a software package developed by Becker (2002) is used for quick-look inspection of data quality at the telescope (P3d_online) or final data reduction (P3d). The code is written in IDL and comprises more than 1200 routines for processing the raw data and subsequent steps of data analysis (e.g., subtracting bias and dark frames, CCD pixel-to-pixel response variation, removal of cosmic rays, tracing, flexure compensation, swath extraction or profile-fitting extraction, stray light modeling, wavelength calibration, and wavelength-dependent fiber response calibration). There are various tools for the visualization of stacked spectra, maps, and individual (or co-added) spectra, for aperture spectrophotometry, data cube PSF-fitting routines, atmospheric dispersion compensation, and so forth (programs monolook, cube_viewer, and many others). Some elements of these tools were found to be useful prototypes for the development of the E3D visualization tool, which is commonly available as open-source code through the Euro3D consortium (Sánchez 2004; Sánchez et al. 2004). The P3d and P3d_online pipelines are accessible through GUIs, facilitating the access of science data and calibration files, and the setup or modification of parameters. It is also possible to operate the pipeline from the IDL command line using scripts instead of the GUI. P3d has also been successfully applied to data other than from PMAS; e.g., for MPFS, SPIRAL, INTEGRAL, and the VIMOS-IFU. More recently, P3d_online was modified to accommodate and visualize data obtained with the new PMAS fiber bundle IFU (PPak_online; see Paper II).

4. INSTRUMENTAL PERFORMANCE

4.1. Assembly, Integration, and Tests

During the development phase, the various subcomponents of PMAS were tested in the laboratory facilities of the AIP. These include tests in the mechanical, optical, and electronics labs, as well as system checks at the AIP telescope simulator. The spectrograph optics were tested at the facilities of Carl Zeiss, Jena, Germany (Roth et al. 2000b; see § 4.2). The image
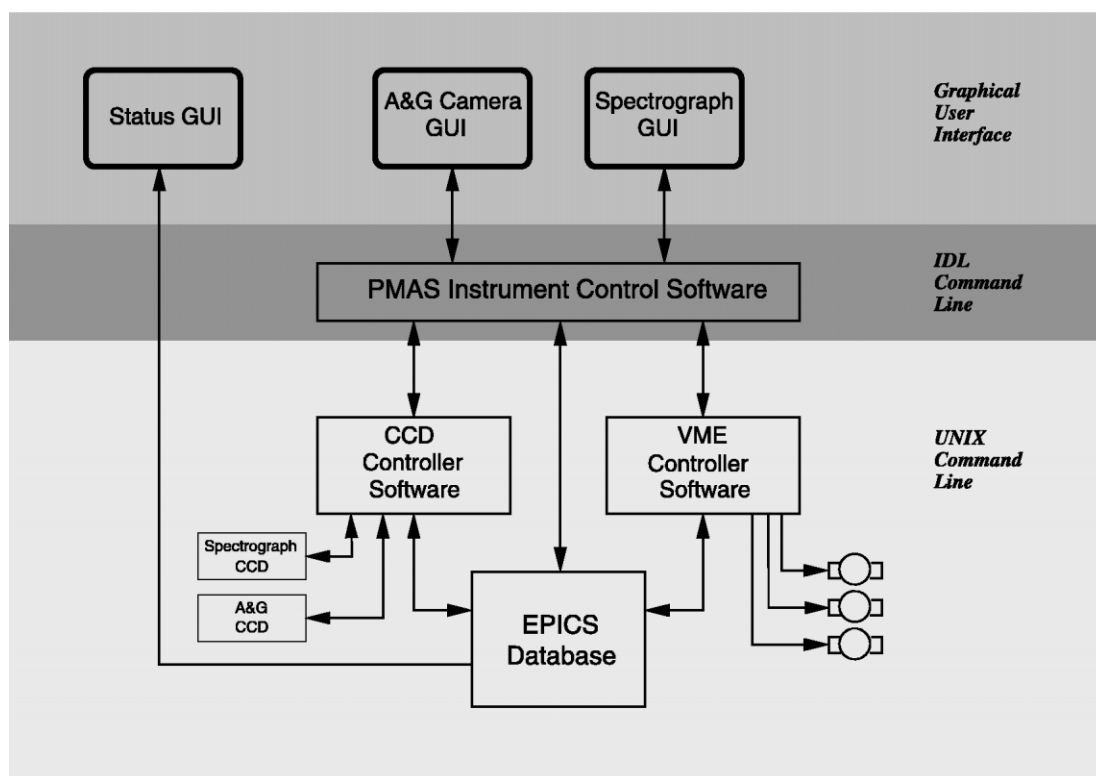
---

[6] See http://www.aps.anl.gov/epics.

Fig. 10.—Diagram of PMAS instrument control software.

quality of all 256 microlenses of the lens array was measured at the AIP (see § 4.3). The complete fore-optics, including the internal calibration unit, were preassembled and tested at the optical laboratory. Extensive fiber tests, including throughput, focal ratio degradation, and stress behavior, were undertaken using a specialized fiber testbench (Schmoll 2001; Schmoll et al. 2003). The three CCD cameras (A&G, single-chip spectrograph, and mosaic spectrograph) were assembled in the detector and clean room facilities and optimized with respect to dark current, readout noise, bias, gain, etc., using the AIP photometric testbench (Fechner et al. 2000). A commercial interferometer was used to assess the optical quality of the folding mirrors, the back side of the lens array, and the Dewar windows.

During the integration of the instrument, PMAS was mostly mounted to the telescope simulator at AIP (Fig. 11). This allowed good access to the instrument, helped in the alignment of the long fore-optics tray, and importantly, provided an option to tip-tilt the instrument. Measurements were taken at various instrument inclinations, often with high spatial magnification, to evaluate the mechanical and thermal stability (see §§ 4.8, 4.9, and 4.10). Using a setup with pinholes and relay lenses, an artificial star was simulated and imaged onto the IFU and the A&G system. The actual spectrograph performance (i.e., PSF, dispersion, coverage, relative grating response, focus behavior, etc.) was measured repeatedly. These measurements were also used to evaluate and optimize the fiber module (i.e.,

the mounting of the fiber slit, the quality of the index matching, the alignment of the lens array, the fiber-to-fiber response, etc.).

4.2. Spectrograph Optics

The spectrograph optical system, consisting of the collimator and camera subsystems, was delivered by the manufacturer with an end-to-end acceptance test that was performed in collaboration with AIP. Details of this test were reported in Roth et al. (2000b), and here we only summarize some key features of the setup and the major results. In the absence of the PMAS spectrograph CCD camera, which was still under development at the time, a commercial cryogenic CCD camera (Photometrics AT200/CE200A) equipped with a blue-sensitive, back side–illuminated TK1024 CCD was used to observe the image of an artificial star in the focal plane of the camera. The spot was enlarged with an $\approx 20 \times$ magnifying microscope objective, yielding a scale of 1.22 ± 0.01 μm pixel^{-1}. The collimator and camera were linearly aligned and illuminated so as to create a spot of controlled size at the collimator input and a uniform illumination at the nominal focal ratio of f/3 in the pupil plane. The results of the image quality tests are listed in Table 4 in terms of diameter of 80% encircled energy.

The overall transmission was not measured end to end, but was estimated from the acceptance test records of the individual lens coatings and from tabulated throughput data for the glasses
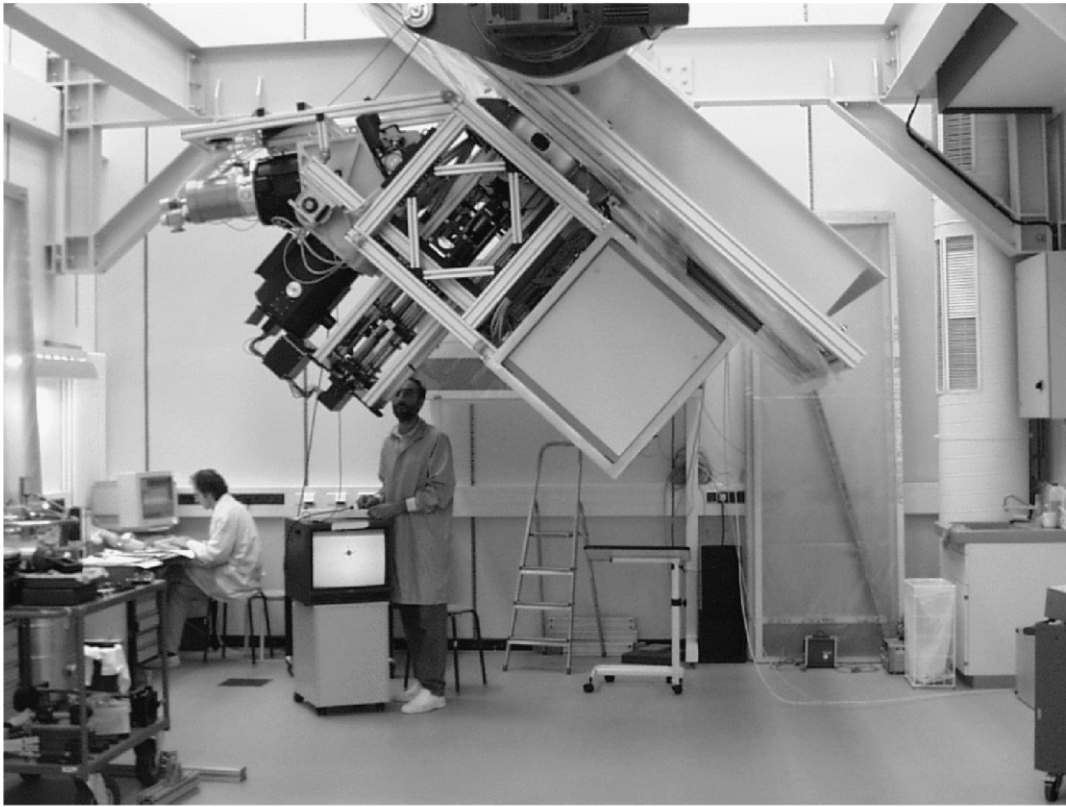
Fig. 11.—PMAS instrument during system performance tests at the AIP telescope simulator. A star simulator can be mounted on top of the device.

and CaF$_2$. The total transmission over the wavelength range 450–1000 nm is ≈80% and almost constant. Toward the blue, it drops nearly linearly to 70% and 55% at 400 and 350 nm, respectively.

A differential flexure test performed at Zeiss by tilting the collimator-camera system with the detector on a rigid platform in 15° steps from 0° to 90° yielded an image shift of 7.5 ± 1 μm over the whole tilt range. The test was reproducible and gave no visible indication of PSF variation. Note that during this test, the linear stages of the focusing lenses (both collimator and camera) were clamped on both sides, thus eliminating additional degrees of freedom. It was discovered later during the PMAS assembly, integration, and test phase that a lack of stability of those mechanisms is responsible for the noticeable flexure of the integrated instrument (see § 4.9).

4.3. Lens Array

The lens array image quality was assessed in lab tests using the same cryogenic camera as described in § 4.2. A 10 μm pinhole was projected to infinity with a f = 160 mm achromatic lens, illuminating the lens array element under study. In its focal plane, a 21 fold demagnified image of the pinhole was observed with the 20 × microscope objective and the CCD camera. Due

to the demagnification, the diameter of the pinhole image is negligible with respect to the Airy pattern of the spot such that the observed figure can be interpreted directly as the PSF of the lenslet. The left frame in Figure 12 shows the superposition of 101 individual exposures of a single spot, which exhibits a very good S/N even at large radii from the centroid of the spot. The PSF core has a FWHM of 4.8 μm. The first Airy diffraction minimum occurs at a radius of ≈4.9 μm. There are significant contributions of diffraction, aberration, and stray light to the extended wings of the PSF at low intensity levels. Figure 13 shows a radial intensity plot of the spot. The dispersion over different azimuthal positions is due to the difference between the enhanced intensity along the pronounced diffraction spikes and the lower intensity in between. Figure 14 shows a normalized curve of growth for the spot, plotting the encircled flux versus radius. The extended parts of the PSF (i.e., diffraction spikes and stray light) make a significant contribution to the total flux. An energy concentration of 80% is reached at a radius of ≈45 μm. By convolving the nominal 43 μm micropupil (0″.5 spaxel^{-1} magnification) with this PSF and measuring the flux within the 100 μm aperture of an ideally centered fiber, we find a typical light loss of 25%–30%. We have measured 80% energy concentration values for all lenslets of the

TABLE 4
ENCIRCLED ENERGY AS FUNCTION OF FIELD ANGLE
AND WAVELENGTH

λ (nm) (1)	$D80$ Design (2)	$D80$+pinhole (3)	$D80$ Measured (4)
0°			
365	18.5	24.5	22.5
436	11.2	17.2	17.5
546	8.5	14.5	17.5
852	12.0	18.5	27.0
3°.5			
365	9.7	15.7	43
436	5.5	11.5	27
546	8.5	14.5	24
852	6.3	12.3	...
4°.9			
365	12.5	18.5	33
436	22.9	28.9	25
546	11.1	16.1	22
852	10.5	16.5	...
6°.0			
365	19.0	25.0	32
436	31.1	37.1	27
546	20.3	26.3	26
852	19.0	25.0	...

NOTE.—Col. (1): wavelength in nm; col. (2): predicted $D80$ according to optical design; col. (3): predicted $D80$, convolved with 10 μm pinhole; col. (4): measured $D80$ ($D80$ = diameter of 80% energy concentration [μm]).
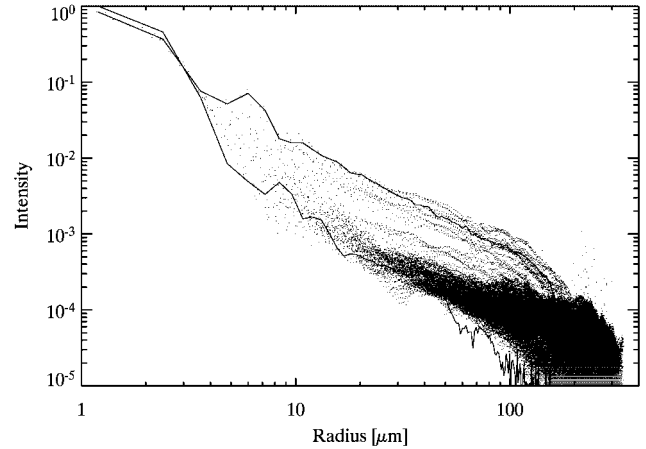
FIG. 13.—Radial plot with normalized intensity of each pixel in Fig. 12 as a function of distance from the center. The upper solid curve follows the intensity along the vertical diffraction spike, the lower curve along a diagonal line with a 45° inclination.

first array delivered, as well as for random selections of lenslets of two 16 × 16 element arrays and of one 32 × 32 element array from a second batch. We determined the following spot concentration statistics for these four devices, respectively: (40-55-65), (30-49-72), (30-57- 70), and (30-51-62), given as 10th-median-90th percentiles for radii of 80% encircled energy (μm). We conclude that the performance is comparable to the "epoxy on glass" type of lens array in the study of Lee et al. (2001), but is a factor of 2 better than the "crossed cylindrical lens" type made from fused silica, a tested device with similar parameters to the PMAS lens array (1 mm pitch, f/5.5). Note that
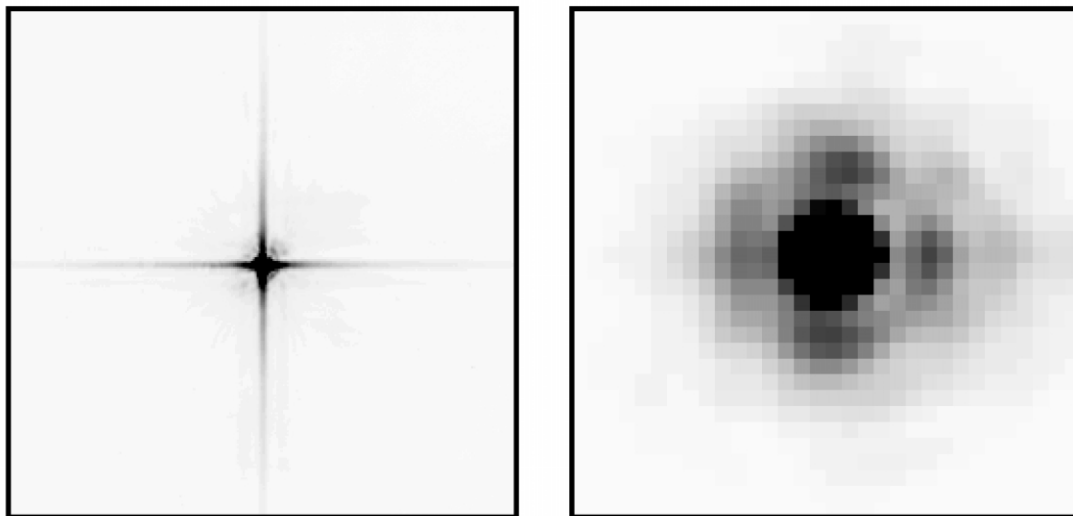

FIG. 12.—Lens array PSF obtained with cryogenic CCD over high dynamic range. *Left*: Single-lenslet PSF averaged from 101 single CCD exposures, gray-scale stretch at 1% peak intensity; frame size: 400 × 400 pixel ≈0.5 × 0.5 mm². *Right*: PSF core detail with Airy pattern, averaged over all 256 lenslets of the whole 16 × 16 lens array.

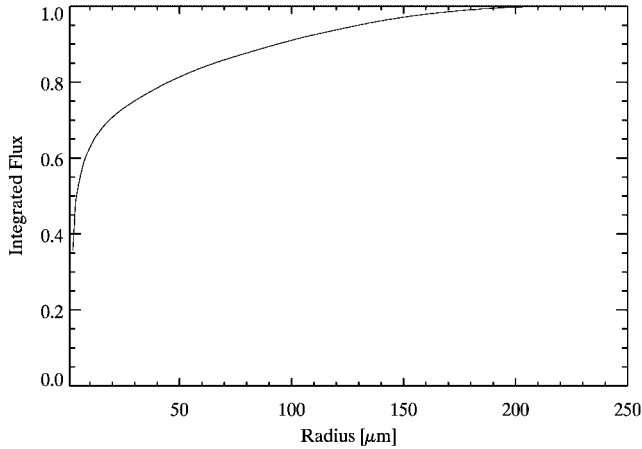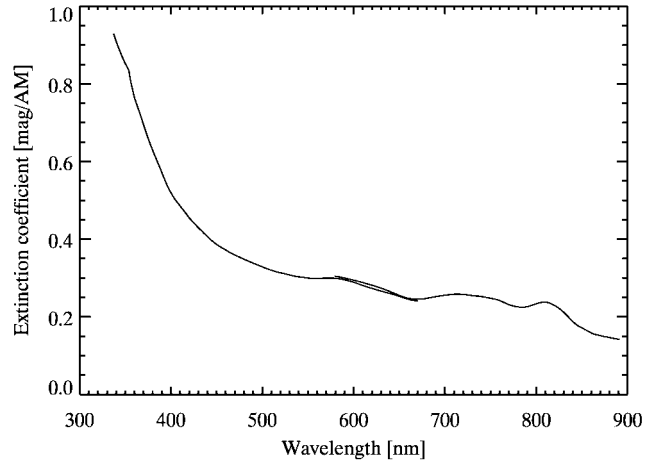FIG. 14.—Encircled energy for the spot shown in FIG. 12.

FIG. 15.—Atmospheric extinction at Calar Alto on 2003 August 1, determined from standard star measurements. The observations cover air masses from 1 to 2 at two wavelength settings (note the overlap at 600 nm). The Calar Alto extinction monitor recorded values between 0.32 and 0.4 mag in *V*.

our results represent upper limits, since the raw frames were not corrected for a possible additional stray light contribution from the microscope objective, as advised by Lee et al. (2001).

4.4. Instrumental Throughput

The instrumental throughput was measured by observing spectrophotometric standard stars and correcting for the atmospheric transmission and reflection losses of the telescope. The observation of flux standards as routinely performed during most observing runs has shown that the atmospheric conditions at Calar Alto are often quite variable, making it difficult to establish a reliable extinction (see also Hopp & Fernandez 2002).[7] On 2003 August 1, however, the flux standard BD +33°2642 (*V* = 10.83; Oke 1990) was observed repeatedly under photometric conditions over the air mass range of 1.0 to 1.95, resulting in an accurate determination of the extinction curve for this night (Fig. 15).

The ratio of observed to expected photons defines the overall efficiency η, which includes the instrument, the atmosphere, and the telescope:

$$\eta = \frac{phot_{obs}(\lambda)}{phot_{exp}(\lambda)} = \eta_{atm}\,\eta_{tel}\,\eta_{instr}. \quad (1)$$

The atmospheric extinction coefficients for each wavelength were calculated in the standard way, using the repeated observations of the star at different air masses (see Fig. 15), which yielded $k_{ext} = 0.3$ mag in *V* and $\eta_{atm} = 0.76$.

The reflectivity of the primary mirror is measured routinely at Calar Alto. Assuming a similar value for the secondary reflectivity, the telescope efficiency was estimated to be

$\eta_{tel} = 0.54$ in *V* at the time of observation. This allowed the determination of the PMAS instrumental response for the setup using the lens array IFU with an $8'' \times 8''$ FOV and the V300 grating. Instrumental throughput values for other configurations were obtained by bootstrapping from this measurement to the relative flux responses of dome-flat exposures, using other gratings that are available for PMAS.

Figure 16 plots the pure PMAS instrumental efficiency η_{instr} (i.e., the throughput from the telescope focal plane to the detector). The maximum efficiency is found to be near 20% at ~600 nm for gratings blazed at *V*. Redward of 600 nm, gratings
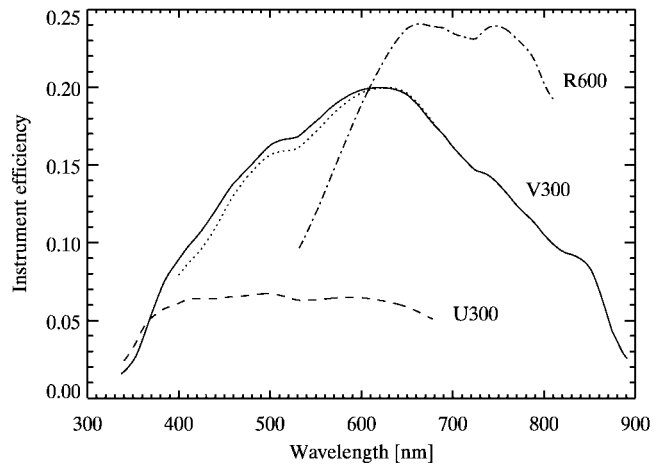

FIG. 16.—Plots of PMAS instrumental efficiencies, indicating the different response of a grating blazed at *V* (*solid curve*), *U* (*dashed curve*), and *R* (*dash-dotted curve*). The efficiency of the V1200 grating (*dotted curve*) is similar to the V300.

---

[7] Calar Alto Newsletter No. 4 (Hopp & Fernandez 2002) is available at http://www.caha.es/newsletter/news02a/boletin4.html.

blazed at R show a peak efficiency of 24%. Gratings blazed at U are superior only at wavelengths below 360 nm. While the throughput depends on the blaze function of the gratings, it is almost independent of the groove density (e.g., 300, 600, or 1200 lines mm^{-1}).

4.5. Fiber-to-Fiber Throughput Variations

Due to the combined effect of less than perfect image quality for individual lens array lenslets, and also alignment, coupling, and the transmission details of individual fibers, there are non-negligible throughput variations from spectrum to spectrum. Figure 17 gives an impression for two groups of 16 spectra, corresponding to slitlet numbers 7 and 8 near the center of the FOV.

Formally, the throughput variation measured from the flux obtained from extracted flat-field spectra amounts to 12% rms for all 256 spectra, or 6% rms if three outlier groups are excluded. This method of characterization, however, is not a fair measure, since the statistical distribution of fiber transmission values is nonnormal, and the systematic effect of vignetting in the fiber spectrograph is not taken into account. We note, rather, that 77% of all spectra are performing with >80% throughput (T), in terms of peak transmission, 17% with $70\% < T < 80\%$, and 6% outliers with $T < 70\%$.

4.6. Spectrophotometric Accuracy

The instrumental accuracy of spectrophotometric measurements is strongly dependent on the reliability of flux calibrations; i.e., the stability between measurements of a science target and the corresponding flux standard(s). Owing to variable atmospheric conditions at the site, an end-to-end validation seemed to be a less than trivial undertaking. Instead, internal spectrophotometric stability tests were taken in the daytime or during nights with poor weather conditions, allowing the telescope to track on an imaginary target for many hours, and taking internal continuum and spectral line lamp exposures with the V300 grating over regular time intervals. Figure 18 illustrates the result from a series of 24 such measurements at a declination of $37°13'$ over an hour angle range of -2^h to $+2^h$.

The continuum flat-field frames were bias-subtracted, traced, extracted, and wavelength-calibrated in the usual way (§ 3.8). The inspection of maps at selected wavelengths (or coadded over wavelength intervals), normalized to the frame taken at HA $= 0^h00^m$, yields varying patterns that are different from unity, indicating that the flat-fielding process was less than perfect. As an example, Figure 18 shows a plot of this variation versus hour angle for the (arbitrarily chosen) fiber number 200. The eight curves were obtained by averaging over 100 spectral pixels each, in increments of 100 pixels from a starting wavelength of ≈ 360 nm. For clarity, the blue bins are plotted as full lines, while the red bins are plotted as dotted lines. The reddening trend toward larger hour angles is seen for all fibers, indicating perhaps a color temperature change of the lamp, and
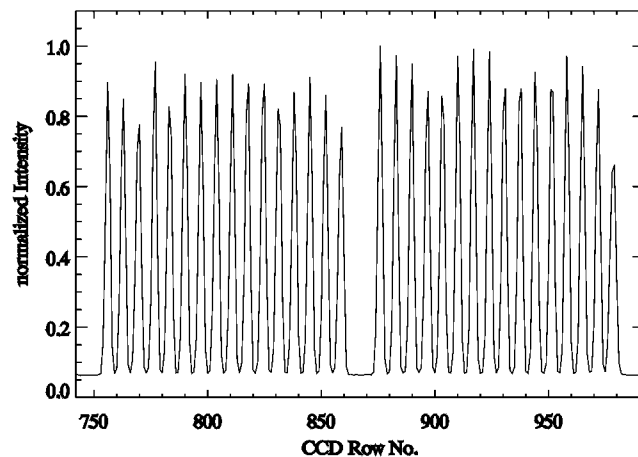

FIG. 17.—Fiber-to-fiber throughput variation for two typical groups of 16 spectra (bias level not subtracted).

not an intrinsic feature of the IFU+fiber bundle. Nonetheless, a systematic variation in any wavelength bin, typically on the order of 1%, is observed over the 4 hr duration of this test. We interpret this variation as the typical accuracy limit for long-term flux calibrations (albeit a caveat regarding the unknown stability of the calibration lamp). As the most likely cause for this behavior, we adopt the hypothesis of a subtle lever effect on the fiber fieldlets (Fig. 7) under a varying-gravity vector, leading to small micropupil-fiber displacements and a subsequent change of the lens array–fiber coupling efficiency. This hypothesis is also supported from a known sensitivity during the (difficult) lens array fiber alignment process.

4.7. Mechanical Stability of the A&G Unit

To evaluate possible flexure effects within the A&G system, which consists of folding mirrors and focusing lenses (§ 3.3), the image motion of an artificial star in the focal plane of the A&G camera was observed as a function of orientation. During tests at AIP, the telescope simulator was moved to a variety of inclinations ranging from $-30°$ to $+45°$. During commissioning at the Centro Astronómico Hispano Alemán (CAHA) 3.5 m telescope, flexure measurements with zenith distances ranging from $0°$ to $63°$ were performed. In both cases, the average image shift was found to be ~0.1 pixel ($= 0.″03$) and ~0.3 pixel ($= 0.″06$) in the x and y direction, respectively. This means that residual-image shifts due to flexure are an order of magnitude smaller than the seeing disk and thus negligible for accurate guiding and offset applications.

4.8. Mechanical Stability of the Telescope Module

The telescope module contains a ≈ 2 m long bench that carries the fore-optics and the lens array IFU. To estimate the flexure of the relatively long optical bench, a finite element analysis
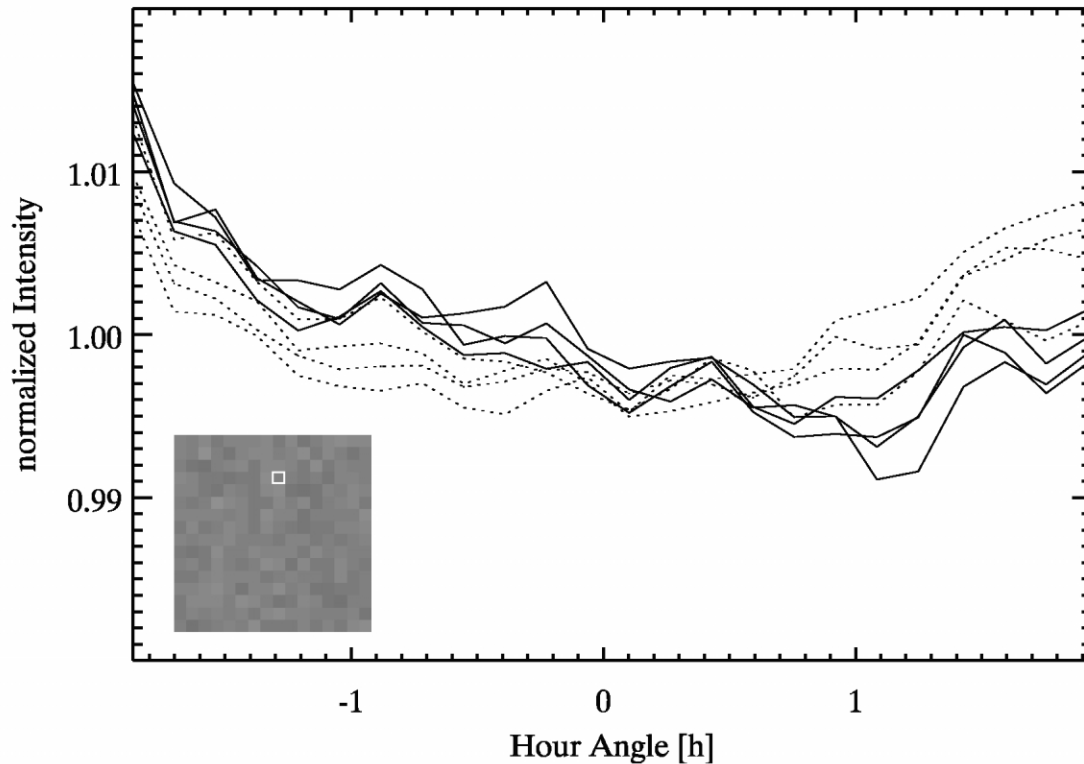
FIG. 18.—Continuum flat-field intensity variation of fiber number 200 for telescope tracking over 4 hr. *Inset*: flat-field map, spaxel number 200 indicated.

(FEA) was performed. In the resulting optimized design, the telescope module tower is mounted to the flange only at its top end, but is not connected to the main frame. The bench structure, together with cover plates, was estimated to exhibit flexure of less than 0.1 mm at a 90° inclination of the instrument (Fig. 19).

During flexure tests at AIP, a star simulator with a variety of pinholes was used to project the image of an artificial star onto the lens array. Spectrograph CCD exposures were taken for various inclinations of the telescope simulator, ranging between −30° and +45°. The image of the star at the IFU was reconstructed, and the centroid was determined. The image shift on the IFU was found to be within ∼0.1 mm, or $\frac{1}{10}$ of a spatial
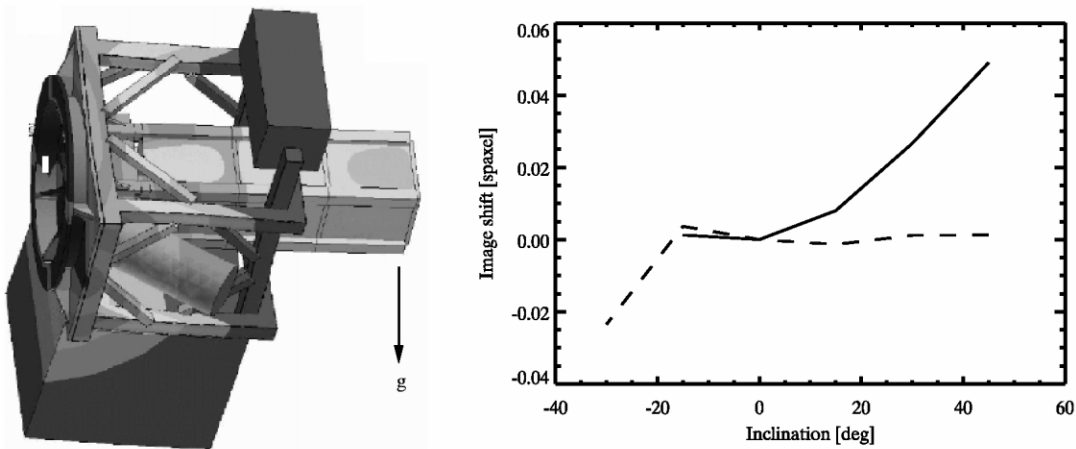

FIG. 19.—*Left*: Telescope module flexure, modeled with ANSYS FEA. The predicted maximum deflection at the end of the telescope module tower at an inclination of 90° is 0.1 mm. *Right*: Measured image shifts in *x* (*solid curve*) and *y* (*dashed curve*) vs. inclination are within a 1/10th of a lens array spaxel.
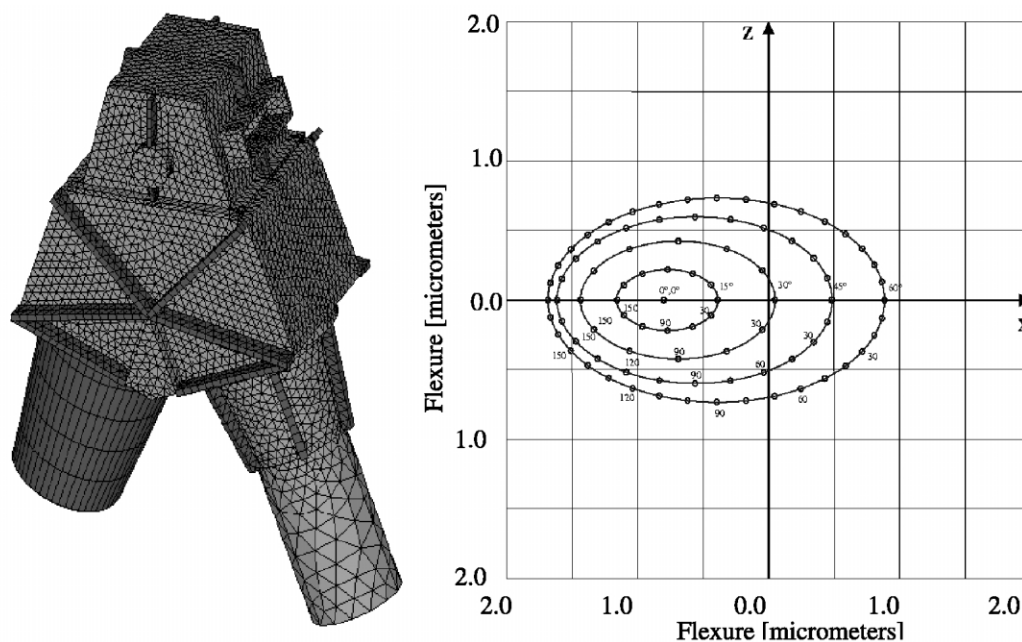
FIG. 20.—*Left*: Model of the stiffness of the spectrograph module, using an ANSYS FE analysis. *Right*: Calculated stiffness of the spectrograph housing, which was expected to be well within 3 μm at all orientations.

element (spaxel), which is in good agreement with the FE model. Depending on the fore-optics magnification, this corresponds to an image motion of 0″.05 to 0″.10; i.e., well below the seeing FWHM.

An analysis of real exposures of point sources observed for half an hour at the telescope revealed no elongation of the images or asymmetries of the PSF that would have been caused by flexure of the fore-optics.

4.9. Mechanical Stability of the Spectrograph

The design of the spectrograph's mechanical structure was also optimized with the help of ANSYS FEAs (Dionies 1998). The final design predicts an image motion of less than 3 μm at any telescope inclination (Fig. 20). Flexure tests undertaken at the AIP telescope simulator revealed considerably larger image shifts than expected, which were found to be caused by the rather unstable focus mechanism of the spectrograph collimator and camera lenses. Since the focus stages are integral parts of the optical subsystems, replacing the poorly performing devices during commissioning was not easily possible and was considered a risk. After some improvement by stiffening the external mechanical interface to the focus stages, the remaining flexure had to be tolerated for the time being.

During some nights of bad weather, flexure tests at the telescope were performed. The telescope was pointed to various (up to 256) positions in hour angle (HA) and declination (decl.). At each pointing, a short arc lamp exposure was taken with the spectrograph CCD, a 1 × 1 binned window around an isolated emission spot was read out, and the resulting image shift was computed.

Figure 21 plots the relative shift of the centroid with respect to its position at zenith (HA = 0^h00^m and δ = +37°.1).

The image shifts in the spectral and the spatial direction differ. Note that the shifts are relatively small for negative hour angles (east of the meridian; rising objects). A significant shift seems to occur during the transit period and for certain positive hour angles (west of the meridian; setting objects). In order to minimize the effects of flexure resulting in a degradation of spectral resolution and an increase of cross talk between adjacent spectra, the critical positions near transit must be avoided during long exposures, or the exposure time must be segmented accordingly.

4.10. Thermal Stability

The variation of the spectrograph best focus as a function of temperature was investigated at the telescope when an extended period of observing nights with identical setup parameters during 2004 November 10–21 presented us with the opportunity to evaluate focus-series measurements taken under similar conditions but at different temperatures. The spot size was measured from the σ provided by Gaussian fits to the emission-line spots in spectral line lamp exposures in the dispersion (X) and spatial (Y) directions. Previous experience with gratings in first order had shown that the two linear stages mounted in the collimator and camera lens barrels show a typical sensitivity of 150 μm travel; from there a significant departure from best focus sets in (10% increase of FWHM). The focusing lens positions in their linear stages are motor-controlled, with a resolution of 1.45 μm per encoder step. The
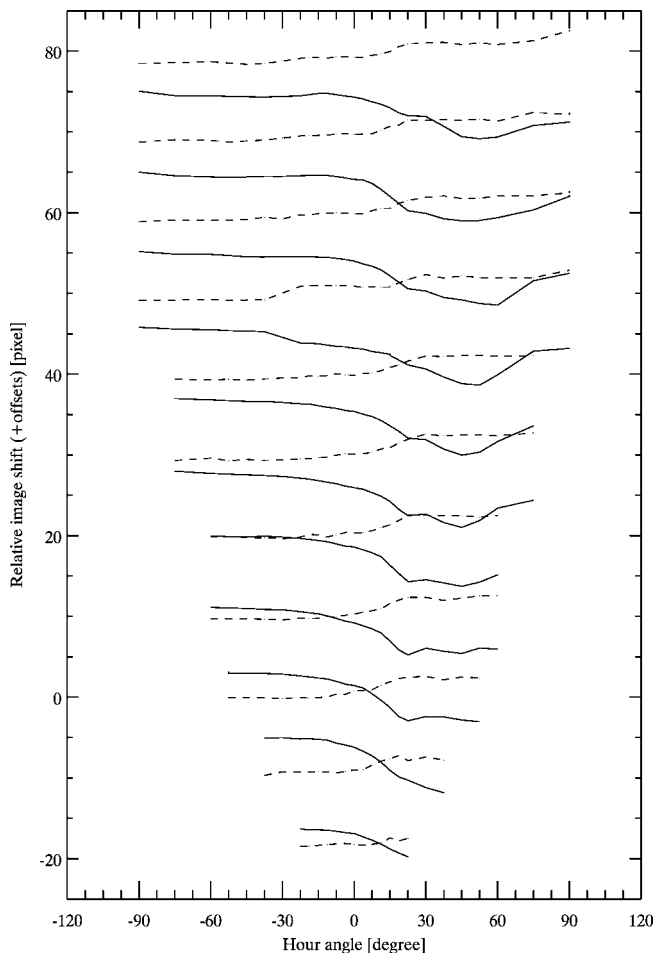
FIG. 21.—Relative image shift in the spectrograph dispersion (*dashed curves*) and cross-dispersion (*solid curves*) direction vs. hour angle (HA). The telescope was moved from east to west at 11 declinations (ranging from $-20°$ to $+80°$). For better clarity, offsets were added for each declination strip. The stability is worse when pointing west of the meridian.

setup for our test was a factor of 3 more sensitive to displacement with respect to FWHM in the dispersion direction, since the J1200 grating in second order was used for medium spectral resolution observations, which benefits from anamorphic demagnification. From the four nights of November 16–19, we were able to compare focus-series measurements over a temperature range of $-2.6°C$, $+0.2°C$, $+2.4°C$, and $+4.0°C$, respectively. The temperature value was taken from the data file FITS header entry for the dome temperature. A typical focus series is evaluated by plotting families of FWHM in X and Y versus camera focus position, labeled by collimator focus position. Depending on a criterion (minimal FWHM in X, in Y, or optimal encircled energy for both directions), the curve presenting the absolute minimum over all pairs of collimator and camera positions is selected, and the minimum parameters are chosen for further use during observations. As a rule of thumb,

the camera focus is roughly a factor of 3 more sensitive to displacement than the collimator. For the thermal variation analysis of best focus, we inspected the focus-series plots for shifts of the minima as a function of temperature. As a result, we find a linear trend at temperatures between $0°C$ and $4°C$, and a steeper gradient toward negative temperatures. Linear regression yields a camera focus shift of $+19.9 \pm 0.7$ μm deg^{-1} at positive temperatures. Below $0°C$, we estimate a rate roughly $3 \times$ larger than this value (however, it is based only on a single data point). We did not recognize a particularly significant temperature dependence of collimator focus over the observed temperature range.

4.11. CCD Performance

The $1K \times 1K$ TK1024 of the A&G CCD system has no major cosmetic flaws and is operated with a conversion factor of $k = 1.4$ e^- ADU^{-1} and a read noise of 4.6 e^-. The quantum efficiency of the chip as specified by the manufacturer is 65% at 400 nm, 80% at 650 nm, and 40% at 900 nm.

The single-chip spectrograph CCD system 1, with its standard gain setting, has a read noise of 4.3 e^- and a conversion factor of 1.4 e^- ADU^{-1}. This CCD is read out over one functional amplifier. It has an approximately circular unresponsive spot ($\approx$45 pixels in diameter) at pixel coordinates (274, 1642), and bad columns beginning at (1624, 2622), (1362, 1232), and (546, 1468). This type of SITe CCD is known to generate spurious charge and exhibit poor CTE performance with excessively fast parallel readout, which is why the chip must be clocked rather slowly. As a compromise, our ST002A is operated with a parallel clock cycle of 800 μs phase^{-1}, which still generates a spurious charge pattern at a rate of $\approx 3 \times 10^{-3}$ e^- row^{-1}. The effect is seen, e.g., in bias frames as a vertical ramp with an amplitude of 12 e^- pixel^{-1}, adding a noise pedestal of 3 e^- in the uppermost rows (and intermediate values below). The chip exhibits another disturbing feature, which was initially seen in bias frames as a bright vertical bar of width $\approx$1100 columns and with an amplitude of 9 e^- pixel^{-1}. This defect, however, disappeared when optimizing the clock pattern during wipe cycles by directing charge transfer *away* from the serial register rather than conventionally *into* it (reverse clocking). The quantum efficiency of the spectrograph camera 1 CCD was measured to be 46%, 65%, and 28%, at the 400, 650, and 900 nm wavelengths, respectively (albeit with the caveat of not having double-checked our laboratory flux standard against an independent secondary calibrator).

The mosaic spectrograph camera 2 combines a science-grade ST002A (readout noise [ron] = 3.8 e^-, $k = 1.36$ e^- ADU^{-1}) with an engineering-grade chip (ron = 9.7 e^-, $k = 1.60$ e^- ADU^{-1}). The former chip has developed a most unfortunate luminescence effect, as described by Janesick (2001), which has prevented us from combining it with the functional CCD of camera 1 (see Roth et al. 2004c for details). Further efforts in optimizing the clock voltages (held in inversion during ex-

posures) have been successful insofar as the luminescence effect has vanished. A residual hot column pattern with a charge level that is extremely sensitive to temperature changes has rendered the mosaic camera unsuitable for faint-object spectroscopy. However, it is still an option for bright targets where wavelength coverage is an issue.

4.12. A&G CCD Photometry and Astrometry

Although the A&G CCD camera was not designed to provide precision photometry in the first place, it is nonetheless considered a potentially useful calibrator for differential spectrophotometry; i.e., correcting for nonphotometric conditions due to thin clouds as put forward, e.g., by Barwig et al. (1987; for a first application with PMAS, see Christensen et al. 2003). With observations of a stellar sequence in field F1038-8 from Stobie et al. (1985), we calibrated the A&G CCD camera with a series of four exposures of 30 s each, obtained on 2002 August 28 at an air mass of 1.17–1.20. We measured star 1 ($V = 12.99$), star 2 ($V = 14.28$), star 4 ($V = 17.94$), star 5 ($V = 18.25$), and star 9 ($V = 20.25$), which are simultaneously visible in the FOV. The exposures were taken through the PMAS V-band filter, which is built according to the recipe by Bessell (1990). Excluding star 9, whose photometry is background limited and thus less suitable for calibration, we fitted the count rates CTS (ADU s^{-1}) from aperture photometry of the four frames and obtained mag $= -2.5$ log CTS $+$ ZP, with a zero point ZP $= -24.225 \pm 0.02$. The 2% error reflects the slightly nonphotometric conditions of the night.

In order to check the optical system of the A&G camera for obvious distortions, archival data from an observing run in 2002 September were analyzed using full-frame acquisition frames from three different fields. The observations were acquired in the PMAS V and R filters, yielding identical results. The astrometry was performed using the Starlink GAIA tool, comparing star detections against DSS plates and the USNO catalog. For each frame, 14–17 stars were found, and their astrometric solution was determined by the program. As a result, the pixel scale was determined to $0\rlap{.}''1966 \pm 0\rlap{.}''0004$ pixel^{-1}. The result is in very good agreement with the design value of $2\rlap{.}''0$ pixel^{-1}. The orientation, whose precise value depends on the position of the Cassegrain flange rotator after instrument changes, was determined to $90\rlap{.}°831 \pm 0\rlap{.}°042$. In practical terms, north appears to the left, east to the bottom when using conventional display tools with CCD pixel (0, 0) at the lower left.

4.13. Operation at the CAHA 3.5 m Telescope

From the spring semester 2001 to fall 2004, PMAS was scheduled for 33 observing runs over a total of 145 nights, and an additional 27 Service A buffer nights for several high-ranked programs. Throughout these observing runs, PMAS worked reliably without any major failure, and not a single night was lost due to technical problems. Some selected science results

from these first years of operation include complete characterization of PSF as sampled by IFU, yielding a centroiding accuracy at a level of 10^{-3} arcsec; application to accurate spectrophotometry of faint, background-limited planetary nebulae in the bulge of M31 (Roth et al. 2004b); PSF-fitting analysis of multiply lensed QSOs (Wisotzki et al. 2003, 2004); first 3D spectrophotometry of a Type Ia supernova (Christensen et al. 2003); 3D spectroscopy of Lyα emitters associated with the DLA system Q2233+131 (Christensen et al. 2004); abundances and kinematics of a candidate sub–damped Lyα galaxy toward PHL 1226 (Christensen et al. 2005); the ultraluminous X-ray source X-1 in Holmberg II (Lehmann et al. 2005); crowded-field 3D spectroscopy of an LBV candidate and circumstellar nebula in M33 (Becker et al. 2004), and others.[8] PMAS has been offered as a common-user instrument under contract with MPIA Heidelberg from the F2002 semester for a period of 3 years and possible future extensions. During this period of operation, PMAS has enjoyed considerable interest from observers, to the extent that it has been the second most demanded instrument at the 3.5 m telescope over the past 2 years.

5. SUMMARY

PMAS is the first dedicated 3D spectrophotometer with low to medium spectral resolution, showing a peak instrumental transmission of 24% and good performance over the whole optical window 0.35–1 μm, especially near the atmospheric cutoff in the blue. The internal accuracy for flux calibrations over several hours is limited to $\approx$1%. The concept of a fiber-coupled lens array type of IFU has proven to be capable of accurately recording the PSF with a centroiding accuracy at the milliarcsec level. PMAS has been used successfully for a variety of astrophysical problems, yielding a number of original publications that have indeed benefitted from the high spatial resolution, 3D spectrophotometry, and the additional information one can retrieve from PSF-fitting techniques. The instrument has been reliably working for over 3 years, without any major failure. Newly installed features include PPak, currently the largest FOV IFU worldwide, a nod-shuffle mode of operation for accurate sky subtraction, and the PYTHEAS mode for an increased spectral resolution over a wide free spectral range. Two underperforming properties, viz., (1) flexure introduced by the unstable focusing stages of the FSPEC optical systems, and (2) rather modest quantum efficiency and overall quality of both the single CCD and the mosaic CCD cameras, are planned to be fixed in a future overhaul and detector upgrade, respectively. The successful exploration of PSF-fitting techniques and crowded-field 3D spectroscopy has important implications for a new generation of advanced 3D spectrographs, such as MUSE for the ESO-VTL (Bacon et al. 2004).

---

[8] See http://www.aip.de/groups/opti/pmas/OptI_pmas.html.

REFERENCES

Allington-Smith, J. R., et al. 2002, PASP, 114, 892

Arribas, S., Mediavilla, E., Garcia-Lorenzo, B., del Burgo, C., & Fuensalida, J. J. 1998, A&AS, 136, 189

Bacon, R., et al. 2004, Proc. SPIE, 5492, 1145

Barwig, H., Schoembs, R., & Buckenmayer, C. 1987, A&A, 175, 327

Becker, T. 2002, Ph.D. thesis, Univ. Potsdam

Becker, T., Fabrika, S., & Roth, M. M. 2004, Astron. Nachr., 325, 155

Bershady, M. A., Andersen, D. R., Harker, J., Ramsey, L. W., & Verheijen, M. A. W. 2004, PASP, 116, 565

Bessell, M. S. 1990, PASP, 102, 1181

Christensen, L., Becker, T., Jahnke, K., Kelz, A., Roth, M. M., Sánchez, S. F., & Wisotzki, L. 2003, A&A, 401, 479

Christensen, L., Sanchez, S. F., Jahnke, K., Becker, T., Wisotzki, L., Kelz, A., Popovic, L., & Roth, M. M. 2004, A&A, 417, 487

Christensen, L., Schulte-Ladbeck, R. E., Sánchez, S. F., Becker, T., Jahnke, K., Kelz, A., Roth, M. M., & Wisotzki, L. 2005, A&A, 429, 477

de Zeeuw, P. T., et al. 2002, MNRAS, 329, 513

Dionies, F. 1998, Ph.D. thesis, Fachhochschule Brandenburg

Eisenhauer, F., et al. 2003, Proc. SPIE, 4841, 1548

Elias, J. H., et al. 1998, Proc. SPIE, 3354, 555

Fechner, T., Wolter, D., & Roth, M. M. 2000, in Proc. 4th ESO CCD Workshop, Optical Detectors for Astronomy II, ed. P. Amico & J. W. Beletic (Dordrecht: Kluwer), 45

Hawarden, T. G., et al. 2003, Proc. SPIE, 4840, 299

Hopp, U., & Fernandez, M. 2002, Calar Alto Newsl., No.4

Kelz, A., Roth, M. M., & Becker, T. 2003a, Proc. SPIE, 4841, 1057

Kelz, A., Roth, M. M., Becker, T., & Bauer, S. 2003b, Proc. SPIE, 4842, 195

Kelz, A., Verheijen, M., Roth, M. M., Laux, U., & Bauer, S. 2004, Proc. SPIE, 5492, 719

Janesick, J. R. 2001, Scientific Charge-coupled Devices (Bellingham: SPIE), 668

Laux, U. 1999, Astrooptik: Optiksysteme für die Astronomie (Heidelberg: Sterne and Weltraum)

Le Coarer, E., Bensammar, S., Compte, G., Gach, J. L., & Georgelin, Y. 1995, A&AS, 111, 359

Lee, D., Haynes, R., Ren, D., & Allington-Smith, J. 2001, PASP, 113, 1406

LeFevre, O., et al. 2003, Proc. SPIE, 4841, 1670

Lehmann, I., et al. 2005, A&A, 431, 847

Lizon, J.-L. 1997, Messenger, 88, 6

Najita, J., & Strom, S. E. 2002, Proc. SPIE, 4835, 1

Oke, J. B. 1990, AJ, 99, 1621

Pasquini, L., et al. 2000, Proc. SPIE, 4008, 129

Reiss, R. 1994, Proc. SPIE, 2198, 895

Roth, M. M. 1990, in ASP Conf. Ser. 8, CCDs in Astronomy, ed. G. H. Jacoby (San Francisco: ASP), 380

Roth, M. M., Becker, T., Böhm, P., & Kelz, A. 2002a, Proc. Scientific Drivers for ESO Future VLT/VLTI Instrumentation, ed. J. Bergeron & G. Monnet (Garching: ESO), 136

———. 2002b, in ASP Conf. Ser. 282, Galaxies: the third Dimension, ed. M. Rosado, L. Binette, L. Arias (San Francisco: ASP), 411

———. 2004a, Astron. Nachr, 2, 147

Roth, M. M., Becker, T., & Kelz, A. 2002c, in ASP Conf. Ser. 282, Galaxies: The Third Dimension, ed. M. Rosado, L. Binette, & L. Arias (San Francisco: ASP), 403

Roth, M. M., Becker, T., Kelz, A., & Schmoll, J. 2004b, ApJ, 603, 531

Roth, M. M., Becker, T., & Schmoll, J. 2000a, in ASP Conf. Ser. 195, Imaging the Universe in Three Dimensions, ed. W. van Breugel & J. Bland-Hawthron (San Francisco: ASP), 122

Roth, M. M., Fechner, T., Becker, T., & Kelz, A. 2004c, Proc. SPIE, 5499, 387

Roth, M. M., Fechner, T., Wolter, D., Kelz, A., & Becker, T. 2002d, Exp. Astron., 14, 99

———. 2004d, Scientific Detectors for Astronomy, The Beginning of a New Era, ed. P. Amico & J. W. Beletic (Dordrecht: Kluwer), 371

Roth, M. M., & Laux, U. 1998, in ASP Conf. Ser. 152, Fiber Optics in Astronomy III, ed. S. Arribas, E. Mediavilla, & F. Watson (San Francisco: ASP), 168

Roth, M. M., Laux, U., & Heilemann, W. 2000b, Proc. SPIE, 4008, 485

Roth, M. M., Laux, U., Kelz, A., & Dionies, F. 2003, Proc. SPIE, 4842, 183

Roth, M. M., Seydack, M., Bauer, S., & Laux, U. 1997, Proc. SPIE, 2871, 1235

Roth, M. M., et al. 2000c, Proc. SPIE, 4008, 277

Sánchez, S. F. 2004, Astron. Nachr., 325, 167

Sánchez, S. F., Becker, T., & Kelz, A. 2004, Astron. Nachr., 325, 171

Schmoll, J. 2001, Ph.D. thesis, Univ. Potsdam

Schmoll, J., Roth, M. M., & Laux, U. 2003, PASP, 115, 854

Schweizer, F. 1979, PASP, 91, 149

Si'lchenko, O., & Afanasiev, V. 2000, A&A, 364, 479

Stobie, R. S., Sagar, R., & Gilmore, G. 1985, A&AS, 60, 503

Verheijen, M. A. W., Bershadey, M. A., Andersen, D. R., Swaters, R. A., Westfall, K., Kelz, A., & Roth, M. M. 2004, Astron. Nachr., 325, 151

Wisotzki, L., Becker, T., Christensen, L., Helms, A., Jahnke, K., Kelz, A., Roth, M. M., & Sanchez, S. F. 2003, A&A, 408, 455

Wisotzki, L., Schechter, P. L., Chen, H.-W., Richstone, D., Jahnke, K., Sánchez, S. F., & Reimers, D. 2004, A&A, 419, L31